

Review

# Progress in Electroreduction of CO<sub>2</sub> to Form Various Fuels Based on Zn Catalysts

Laxia Wu <sup>1</sup>, Lin Wu <sup>1</sup>, Chang Guo <sup>1</sup>, Yebin Guan <sup>1</sup>, Huan Wang <sup>2,\*</sup> and Jiaying Lu <sup>2,\*</sup>

<sup>1</sup> Anhui Province Key Laboratory of Optoelectronic and Magnetism Functional Materials, School of Chemistry and Chemical Engineering, Anqing Normal University, Anqing 246011, China; wulaxia.1230@163.com (L.W.); wulin@aqnu.edu.cn (L.W.); gaochang@aqnu.edu.cn (C.G.); guanyb@aqnu.edu.cn (Y.G.)

<sup>2</sup> Shanghai Key Laboratory of Green Chemistry and Chemical Processes, School of Chemistry and Molecular Engineering, East China Normal University, Shanghai 200062, China

\* Correspondence: hwang@chem.ecnu.edu.cn (H.W.); jxlu@chem.ecnu.edu.cn (J.L.)

**Abstract:** Carbon dioxide (CO<sub>2</sub>) is one of the main greenhouse gases and the major factor driving global climate change. From the viewpoint of abundance, economics, non-toxicity, and renewability, CO<sub>2</sub> is an ideal and significant C1 resource, and its capture and recycling into fuels and chemical feedstocks using renewable energy is of great significance for the sustainable development of society. Electrochemical CO<sub>2</sub> reduction reactions (CO<sub>2</sub>RRs) are an important pathway to utilize CO<sub>2</sub> resources. Zinc has been demonstrated as an effective catalyst for CO<sub>2</sub>RRs. Numerous studies have focused on improving the efficiency of zinc-based catalysts by tuning their morphology and components, as well as controlling their oxidation states or doping. However, only a handful of reviews have evaluated the performance of Zn-based CO<sub>2</sub>RR electrocatalysts. The present review endeavors to fill this research gap and introduces the recent progress in using CO<sub>2</sub>RRs to create various fuels (carbon-containing substances or hydrocarbons) using zinc-based catalysts, including Zn monomers, Zn-containing bimetals, oxide-derived Zn catalysts, and single/dual Zn atom catalysts. The mechanism of the electroreduction reaction of CO<sub>2</sub> is discussed. Based on the previous achievements, the current stage and the outlook for future developments in the field are summarized. This review will provide a reference for future research on CO<sub>2</sub>RRs to generate fuels using Zn-based catalysts and their commercialization.

**Keywords:** CO<sub>2</sub>RR; Zn-based catalyst; electrocatalyst; fuels; CO<sub>2</sub> utilization



**Citation:** Wu, L.; Wu, L.; Guo, C.; Guan, Y.; Wang, H.; Lu, J. Progress in Electroreduction of CO<sub>2</sub> to Form Various Fuels Based on Zn Catalysts. *Processes* **2023**, *11*, 1039. <https://doi.org/10.3390/pr11041039>

Academic Editor: Farooq Sher

Received: 24 February 2023

Revised: 22 March 2023

Accepted: 27 March 2023

Published: 29 March 2023



**Copyright:** © 2023 by the authors. Licensee MDPI, Basel, Switzerland. This article is an open access article distributed under the terms and conditions of the Creative Commons Attribution (CC BY) license (<https://creativecommons.org/licenses/by/4.0/>).

## 1. Introduction

With the rapid development of the global economy, atmospheric pollution is becoming more and more serious [1]. In particular, the emissions of harmful gases not only cause severe atmospheric pollution in local areas, but also seriously affect global climate change. Various environment-related global problems, such as the greenhouse gas effect, acid rain, and the depletion of the ozone layer, have emerged, which seriously threaten the living and development spaces of human beings [2].

Energy is the basis of social development and can be divided into renewable and non-renewable energy sources. Non-renewable energy sources, especially fossil fuels, are the most dominant in our present energy infrastructure [3]. Since industrialization, fossil fuels have been a major driving force for the development of human society, and more than 80% of primary energy requirements have been derived from fossil fuels. Large-scale consumption of fossil-based energy inevitably leads to larger emissions of greenhouse gases, including CO<sub>2</sub> [4]. At present, the global annual carbon emissions generated by the combustion of fossil fuel have reached a gigaton scale. Correspondingly, atmospheric CO<sub>2</sub> concentration has increased by 49.3% from 280 ppm in 1750 to 418 ppm in 2022 [5].

In order to mitigate or even reverse this trend, humans not only have to change their energy consumption patterns, but they also have to develop economically viable technolo-

gies to capture and utilize carbon dioxide from the atmosphere [6–8]. The technologies that have been proposed to achieve this follow one of two approaches: carbon capture and storage (CCS) or carbon capture and utilization (CCU) [9]. CCS is a method to reduce CO<sub>2</sub> emissions. However, huge investment requirements, high energy consumption, CO<sub>2</sub> leakage, and the unsustainability of CCS technology hinder its practical application worldwide. CCU involves CO<sub>2</sub> capture, the direct utilization of CO<sub>2</sub> (for example, in soft drinks or fire extinguishers), or the conversion of CO<sub>2</sub> into chemicals or fuels. In today's world of high energy demand, CCU seems to be a more attractive and promising solution than CCS. So far, various CO<sub>2</sub> conversion pathways have been explored, such as chemical reforming, as well as biological, photochemical, and electrochemical methods [10–12]. Among them, the electrochemical pathway is the most attractive, because it activates CO<sub>2</sub> by directly importing clean and renewable electrical energy such as solar, wind, and hydroelectric. Electrochemical CO<sub>2</sub> reduction reactions (CO<sub>2</sub>RRs) are an important route to realizing the reaction between CO<sub>2</sub> and water, in which C-H and C-C bonds are established to form hydrocarbons, acids, and alcohols [13]. CO<sub>2</sub>RRs have the potential to provide a sustainable pathway to produce many of the world's most-needed commodity chemicals (Figure 1) [8].

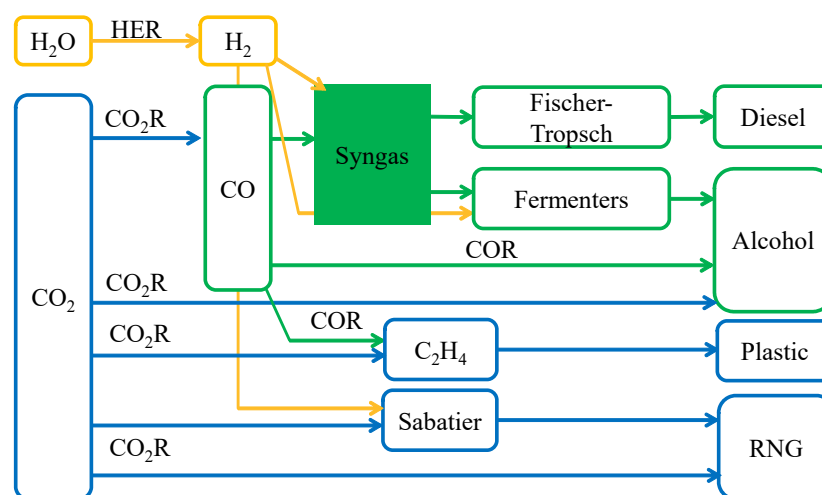


**Figure 1.** Possible renewable-energy-powered routes to create commodity chemicals driven by electrocatalysis from H<sub>2</sub>O (yellow) and CO<sub>2</sub> (green, blue) as feedstocks [8]. Reprinted with permission from Ref. [8]. Copyright © 2023, The American Association for the Advancement of Science.

At present, CO<sub>2</sub>RRs face several challenges. Firstly, CO<sub>2</sub> has a linear molecular structure with two stable C = O bonds, and its thermodynamic stability makes the reduction kinetically sluggish. Secondly, various reaction pathways for CO<sub>2</sub> reduction limit the selectivity of the reaction [14]. In addition, a hydrogen evolution reaction (HER) [15] always exists as a competitive side reaction and tends to be kinetically more favorable than CO<sub>2</sub>RR [16]. Therefore, the development of suitable electrocatalysts to significantly accelerate the reaction rate and shift the reaction selectivity toward the target products is urgently needed. In the 1980s, Hori et al. reported a pioneering work on CO<sub>2</sub>RRs using metal electrodes [17]. Since then, different electrocatalysts, including molecular, heterogeneous, and hybrid catalysts, have been designed and used in the electrochemical reduction of CO<sub>2</sub> [18]. Generally, catalysts can be divided into metal catalysts and non-metallic catalysts. Metal catalysts include noble metal catalysts and non-noble metal catalysts. Noble metals, such as Au [19–21], Ag [22–24], and Pd [25,26], have been reported as highly efficient electrocatalysts for the selective conversion of CO<sub>2</sub> to CO. Their structures and morphologies affect the Faraday efficiency and current density of CO<sub>2</sub> conversion to CO. However, the scarcity of noble metals and related high costs inevitably limit their large-scale applications. Among various non-noble metal candidates, Zn has attracted the

attention of researchers due to its cost-effectiveness, well-defined structure, high surface-to-volume ratio, and high selectivity for CO in CO<sub>2</sub>RRs.

In the present review, the recent progress in the reduction of CO<sub>2</sub> to different fuels using Zn-based electrocatalysts is discussed. The fundamentals of CO<sub>2</sub>RRs, including the electrochemical behavior of electrocatalysts, experimental procedures, product analysis, and possible reaction pathways, have been discussed. Then, various Zn-based catalysts such as Zn monomers, Zn-containing bimetals, oxide-derived Zn catalysts, and single/dual Zn atom catalysts, as well as related research achievements, are elaborated. Finally, existing challenges and future developments and opportunities in this field are also summarized.

## 2. Fundamentals of the Electroreduction of CO<sub>2</sub>

### 2.1. Electrochemical Behavior of Electrocatalysts

#### 2.1.1. Cyclic Voltammetry

Cyclic voltammetry experiments require the setting of the three most basic parameters: the potentials of the upper limit, the potentials of the lower limit, and the scan rate. Upper and lower potential limits are determined based on the electrochemical window of the solvent (e.g., water) and the stability of the electrode material. The potential scan rate is determined according to the reaction type and testing method. The scan rate can usually be above 50 mV·s<sup>-1</sup> for the liquid phase; however, it should not exceed 20 mV·s<sup>-1</sup> during steady-state measurements.

The electrochemical voltametric behavior of electrocatalysts is generally determined as follows: A three-electrode system with platinum mesh is used as a counter electrode. A saturated calomel electrode (SCE) is used as the reference electrode, whereas a catalyst-coated substrate electrode (such as a glassy carbon electrode) is used as the working electrode. These electrodes are used in an undivided cell at normal temperature and pressure. The voltammograms are recorded using an electrochemical workstation under sequential N<sub>2</sub> and CO<sub>2</sub> bubbling.

#### 2.1.2. Electrochemical Activity Surface Area (ECSA) Characterization

The surface structure of the electrode significantly influences its catalytic performance. Electrodes are usually solid, though the structure of the solid surface is complex. Moreover, there are many types of surface sites (such as platforms, steps, kinks and vacancies, and different structures of the atomic arrangements). The structural information of the electrode surface can be obtained using electrochemical measurements. Atoms, molecules, and ions (such as H, O, CO) that interact strongly with the surface are selected to characterize the surface structure of the electrodes by using their adsorption–desorption characteristics and oxidative removal.

Hydrogen adsorption on the platinum surface consists of monolayer adsorption, which means that one platinum atom corresponds to one adsorbed hydrogen atom. Therefore, the ECSA of platinum can be calculated based on the amounts of charge on the adsorbed and desorbed hydrogen. For platinum alloys, the values of the ECSA calculated using this method tend to be small, because alloying elements can inhibit the adsorption and desorption of hydrogen. Moreover, CO can produce strong adsorption on a variety of metal surfaces. Therefore, CO stripping curves are often used to measure the ECSA of metals, especially platinum group metals and their alloys. For coin elements such as gold, silver, and copper, the adsorption capacities of both H and CO are not strong, and the underpotential deposition of metals such as Pb and Cu is often used to calculate the ECSA.

### 2.2. Experimental Procedures and Product Analysis

#### 2.2.1. Experimental Procedures

Three types of electrocatalytic reactors are used for CO<sub>2</sub>RRs and include the H-cell, the flow cell, and the membrane electrode assembly (MEA) cell [27]. Among them, the H-cell is the most commonly used in fundamental studies mainly because of its low cost and simple operation [28]. In this section, the setup of the H-cell and the experimental procedure for

electrocatalysis are briefly described. Typically, a CO<sub>2</sub>RR is carried out using potentiostatic electrolysis in a two-compartment electrochemical cell using a standard three-electrode system. The working electrode is usually a catalyst-coated carbon paper, a glassy carbon electrode, a glassy carbon plate, or a carbon fiber paper. The working and reference electrodes are placed in the cathode compartment, whereas the counter electrode is placed in the anode compartment. The two compartments are separated by an ion exchange membrane. A proton exchange membrane is taken as an example in Figure 2. Aqueous solutions of NaHCO<sub>3</sub> or KHCO<sub>3</sub> are often chosen as electrolytes. When saturated with CO<sub>2</sub>, an electrolyte can effectively buffer the change in pH of the bulk solution and keep it to near-neutral. The reduction in CO<sub>2</sub> occurs at the cathode, whereas the oxidation of oxygen (coming from water) occurs at the anode. H<sup>+</sup> ions migrate to the cathode through a proton exchange membrane under the action of an electric field, thereby providing a source of hydrogen for the reduction of the carbon dioxide. Thermodynamically, for the electroreduction of CO<sub>2</sub> at different potentials, different multiple electron transfer reactions can occur and include the transfer of 2e<sup>-</sup>, 4e<sup>-</sup>, 6e<sup>-</sup>, 8e<sup>-</sup>, 12e<sup>-</sup>, and so on while also generating different reduction products. At present, the reported products of the electroreduction of CO<sub>2</sub> mainly include carbon monoxide (CO) [29–31], methane (CH<sub>4</sub>) [32], methanol (CH<sub>3</sub>OH) [33,34], formic acid/formate (HCOOH/HCOO<sup>-</sup>) [14,35], ethylene (C<sub>2</sub>H<sub>4</sub>) [36,37], ethane (C<sub>2</sub>H<sub>6</sub>), ethanol (C<sub>2</sub>H<sub>5</sub>OH) [38–40], acetic acid/acetate (CH<sub>3</sub>COOH/CH<sub>3</sub>COO<sup>-</sup>) [41], and *n*-propanol (CH<sub>3</sub>CH<sub>2</sub>CH<sub>2</sub>OH) [42]. The electrochemical half reactions generating these products, along with the corresponding standard redox potentials, are listed in Table 1 [43].

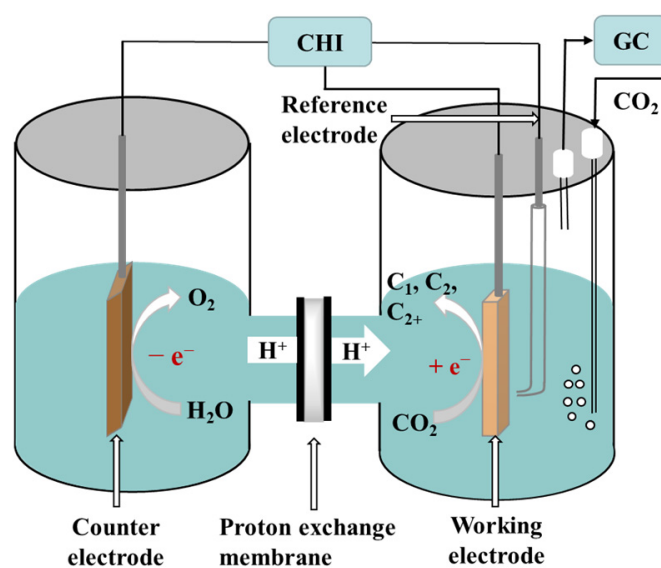


**Figure 2.** Schematic of electroreduction of CO<sub>2</sub> in the H-cell.

**Table 1.** Electrochemical potentials of possible CO<sub>2</sub>RRs in aqueous solutions [43].

Products	Equation	$E^\ominus$ (V vs. RHE)
Hydrogen	$2\text{H}^+ + 2\text{e}^- \rightarrow \text{H}_2$	0.000
Carbon monoxide	$\text{CO}_2 + 2\text{H}^+ + 2\text{e}^- \rightarrow \text{CO} + \text{H}_2\text{O}$	-0.104
Methane	$\text{CO}_2 + 8\text{H}^+ + 8\text{e}^- \rightarrow \text{CH}_4 + \text{H}_2\text{O}$	0.169
Methanol	$\text{CO}_2 + 6\text{H}^+ + 6\text{e}^- \rightarrow \text{CH}_3\text{OH} + \text{H}_2\text{O}$	0.016
Formic acid/formate	$\text{CO}_2 + 2\text{H}^+ + 2\text{e}^- \rightarrow \text{HCOOH}$	-0.171
Ethylene	$\text{CO}_2 + 12\text{H}^+ + 12\text{e}^- \rightarrow \text{C}_2\text{H}_4 + 4\text{H}_2\text{O}$	0.085
Ethane	$\text{CO}_2 + 14\text{H}^+ + 14\text{e}^- \rightarrow \text{C}_2\text{H}_6 + 4\text{H}_2\text{O}$	0.144
Ethanol	$2\text{CO}_2 + 12\text{H}^+ + 12\text{e}^- \rightarrow \text{CH}_3\text{CH}_2\text{OH} + 3\text{H}_2\text{O}$	0.084
Acetic acid/acetate	$2\text{CO}_2 + 8\text{H}^+ + 8\text{e}^- \rightarrow \text{CH}_3\text{COOH} + 2\text{H}_2\text{O}$	0.098
<i>n</i> -Propanol	$3\text{CO}_2 + 18\text{H}^+ + 18\text{e}^- \rightarrow \text{CH}_3\text{CH}_2\text{CH}_2\text{OH} + 5\text{H}_2\text{O}$	0.095

### 2.2.2. Qualitative and Quantitative Analyses of Products

After electrolysis, the catholyte is transferred to a headspace sample injector, while the liquid products, such as methanol, ethanol, and acetone, are detected using gas chromatography. Comparing the product's peak position with that of the standard sample allows for qualitative judgment of the liquid products. The liquid product can also be quantified using  $^1\text{H}$  NMR spectroscopy.

The gas products (such as  $\text{H}_2$ ,  $\text{CO}$ ,  $\text{CH}_4$ , and  $\text{C}_2\text{H}_4$ ) generated during electrolysis are collected using a gas sampling bag. At the time of detection, gas is injected into the gas chromatograph with a syringe. Comparing the retention times of products obtained using gas chromatography with those of standards allows for qualitative judgment of the gas products. A standard curve is plotted according to the peak area of the produced gas chromatogram of the standard gas and the concentration of each component in the gas. The Faraday efficiency of the products can be quantitatively calculated according to Equation (1) [44].

$$FE = \frac{\phi v t z F}{Q V_m} \quad (1)$$

where  $\phi$  is the volume fraction of gas products in the total gas, which can be obtained from the standard curve,  $v$  is the flow rate of  $\text{CO}_2$  ( $\text{L} \cdot \text{min}^{-1}$ ),  $t$  is the electrolysis time (min),  $z$  is the number of electrons transferred in a specific electrode reaction, as shown by the data presented in Table 1 (for example,  $z = 2$  for a  $\text{CO}_2\text{RR}$  to  $\text{CO}$ ),  $F$  is the Faraday constant with the value of  $96,485 \text{ C} \cdot \text{mol}^{-1}$ ,  $Q$  is the total amount of electricity in the electrolysis process (C), and  $V_m$  is the molar volume of gas at  $25^\circ\text{C}$  and standard pressure.

### 2.3. Reaction Mechanism of $\text{CO}_2\text{RRs}$

The electroreduction of carbon dioxide is a process in which reduction occurs by  $\text{CO}_2$  molecules or  $\text{CO}_2$ -solvated ions acquiring electrons from the electrode's surface within the solution. Electroreduction is a multistep process involving the transfer of multiple electrons, and it consists of  $\text{CO}_2$  adsorption, electron transfer, and product desorption at the electrode surface. A large number of studies have shown that the current density, species, and selectivity of the  $\text{CO}_2\text{RR}$  are largely dependent on the electrode material and the reduction potential. The electrocatalysis of carbon dioxide undergoes different reaction pathways to generate different products. Figure 3 shows the main pathways for the electroreduction of  $\text{CO}_2$  [45].

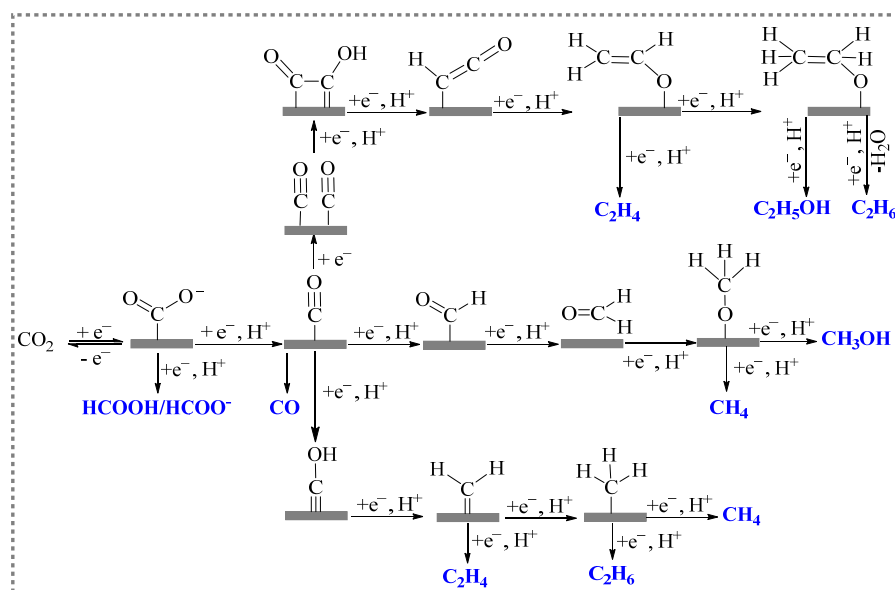


**Figure 3.** Possible reaction pathways for the electroreduction of  $\text{CO}_2$ .

The CO<sub>2</sub> molecule is first adsorbed onto the surface of the catalyst, and, then, it is activated to absorb carbon dioxide (\*CO<sub>2</sub><sup>-</sup>), which generates into intermediate \*COOH through proton transfer. The intermediate \*COOH undergoes another proton transfer and eventually generates HCOOH. The formation pathway of CO is similar to that of formic acid. Meanwhile, the intermediate \*COOH is further reduced to form adsorbed CO (\*CO). \*CO is a relatively important intermediate that undergoes a series of electron transfer and protonation processes to generate different reduction products. For the generation of CH<sub>4</sub>, the \*CO is hydrogenated in C or O to generate \*CHO or \*COH. In the \*CHO pathway, the configurations of adsorbed intermediates change from C binding in \*CHO to O binding in \*OCH<sub>2</sub>. Moreover, \*OCH<sub>3</sub>, and gaseous CH<sub>4</sub> with \*O are obtained on the surfaces of the catalysts. The other pathway of \*COH involves the formation of adsorbed C (\*C). The \*C is further reduced to \*CH, \*CH<sub>2</sub>, \*CH<sub>3</sub>, and finally to CH<sub>4</sub>. The formation of C<sub>2</sub>H<sub>4</sub> or other hydrocarbons requires controlled coupling reactions between CHO\* and CH<sub>2</sub>O\* into \*OCH-CHO\*, \*OCH-CH<sub>2</sub>O\*, or \*OCH<sub>2</sub>-CH<sub>2</sub>O\*, which is then followed by hydrogenation/dehydration reactions [46,47].

It is generally believed that the selectivity of the products of the electroreduction of CO<sub>2</sub> depends on the binding energy between the electrocatalytic materials and the reaction intermediates such as \*CO, CO<sub>2</sub><sup>-</sup>, \*COOH. When CO<sub>2</sub> is reduced to CO on the surface of electrodes, the binding energy between the electrode material and the CO determines the selectivity of the products generated during electrocatalytic reduction. The electrocatalytic products of electrodes (such as Ag, Au, and Zn) with weak CO binding tend to have high CO selectivity. Moreover, the CO generated during the reduction reaction is easily separated from the electrode surface and does not enter into the next reduction reaction. Various electrode materials (such as Pt, Fe, Co, and Ni) have stronger binding energies for CO, and, therefore, almost no CO<sub>2</sub> reduction products are produced when using these materials. This is because, after its generation, CO forms strong interactions with the metal sites on the surface, and the next reduction reaction cannot proceed as a result. Meanwhile, H<sup>+</sup> reduction dominates, and a hydrogen evolution reaction occurs. Some electrode materials have moderate binding energies for the intermediates (such as \*CO, CO<sub>2</sub><sup>-</sup>, and \*COOH) due to the coincidence that the intermediates are stabilized. This, in turn, prompts the generation of reduction products with more than two electron transfers. C-C coupling reaction may also occur to yield C<sub>2+</sub> products.

### 3. Zn-Based Catalysts for CO<sub>2</sub>RRs

#### 3.1. Zinc Monomer Catalyst

##### 3.1.1. Zinc Monomer Catalyst for CO<sub>2</sub> Reduction to CO

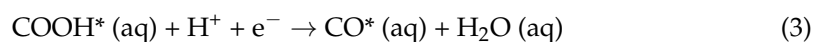
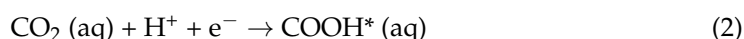
Zinc (Zn) holds the promise as a potential alternative to noble metals because of its abundance and intrinsic selectivity towards CO production [17]. However, the activity and CO selectivity of Zn are relative lower than those of Au and Ag catalysts [48]. To overcome these limitations, many efforts have been devoted to synthesizing nanostructured zinc catalysts. Various strategies, including electrodeposition, anodization, and oxide reduction, have been employed (Table 2). When compared to bulk Zn electrodes, the obtained nanostructured Zn [49–52] exhibits higher catalytic activity and CO selectivity. For example, nanostructured Zn dendrite electrocatalysts obtained using electrodeposition exhibited a catalytic activity that was one order of magnitude higher than that of bulk zinc foil and also enhanced the Faraday efficiency of CO by more than 2-fold [49]. Nanoscale Zn obtained using anodization and electroreduction was used for a CO<sub>2</sub> reduction reaction to CO in an aqueous NaCl solution, where it obtained a Faraday efficiency of up to 93% [53]. Sharp zinc nanowires prepared using a hydrothermal method exhibited an excellent selectivity of 98% and stability for 35 h during the electroreduction of CO<sub>2</sub> to CO in aqueous electrolytes under ambient conditions [54]. A hierarchical hexagonal Zn catalyst (*h*-Zn) obtained using the electrodeposition of a ZnCl<sub>2</sub> solution on Zn foil was used for a CO<sub>2</sub> reduction reaction to CO [50]. Based on Woo's linear voltammetry results, the *h*-Zn exhibited a higher current density than that of Zn foil (Figure 4a).

**Table 2.** A summary of Zn monomer catalysts for CO<sub>2</sub>RRs to CO.

Electrocatalyst	Method	Durability	Potential/V <sub>RHE</sub>	Current Density	Electrolyte	FE <sub>CO</sub>	Ref
Dendritic Zn	Electrodeposition	3 h	−1.10	13 <sup>b</sup> mA·cm <sup>−2</sup>	0.5 M NaHCO <sub>3</sub>	79%	[49]
Hexagonal Zn	Electrodeposition	30 h	−0.85 −1.05	9.5 mA·cm <sup>−2</sup> 5.6 mA·cm <sup>−2</sup>	0.5 M KHCO <sub>3</sub> 0.5 M KCl	85.4% 95.4%	[50]
H-Zn-NPs	Electrodeposition and reduction	12 h	−0.96	5.3 mA·cm <sup>−2</sup>	0.1 M KHCO <sub>3</sub>	94.2%	[51]
Porous Zn	Electrodeposition	6 h	−0.95 −1.0 −0.8	27 mA·cm <sup>−2</sup> 20 mA·cm <sup>−2</sup> 25.6 mA·cm <sup>−2</sup>	0.1 M KHCO <sub>3</sub> 0.5 M KCl 0.5 M NaHCO <sub>3</sub>	94.4% 91.8% 73.1%	[52]
Zn Nanoplates	Anodized and electroreduction	10 h	−1.10 <sup>a</sup>	15 <sup>b</sup> mA·cm <sup>−2</sup>	0.5 M NaCl	93%	[53]
Zinc Nanowires	Hydrothermal electroreduction	35 h	−0.95	40 mA·cm <sup>−2</sup>	0.5 M KHCO <sub>3</sub>	98%	[54]
Zn Nanopore	Cathodic	-	−1.21 <sup>a</sup>	15.1 mA·cm <sup>−2</sup>	0.25 M K <sub>2</sub> SO <sub>4</sub>	92%	[55]
RE-Zn-CO <sub>2</sub>	electrodeposition	-	−1.10	16.2 mA·cm <sup>−2</sup>	0.5 M KHCO <sub>3</sub>	69.6%	[56]
RE-Zn-CO <sub>2</sub> /KCl	electrodeposition	20 h	−1.05	4.3 mA·cm <sup>−2</sup>	0.5 M KCl	95.9%	[56]
LiET-Zn	Li electrochemical tuning	4 h	−1.17	26.5 mA·cm <sup>−2</sup>	0.1 M KHCO <sub>3</sub>	91.1%	[57]
Zn NPs (6.8 nm)	Inverse micelle encapsulation	-	−1.10	4 <sup>b</sup> mA·cm <sup>−2</sup>	0.1 M KHCO <sub>3</sub>	70%	[58]
Multilayered Zn Nanosheets	Electrochemical reduction	7 h	−1.13	14 mA·cm <sup>−2</sup>	0.5 M NaHCO <sub>3</sub>	86%	[59]
Zn Nanoflakes	Electrodeposition	-	−0.9	~4.9 <sup>b</sup> mA·cm <sup>−2</sup>	0.1 M KHCO <sub>3</sub>	~43% b%	[60]
Porous Zn	Anodized and then reduction	2 h	−0.79	~1.3 <sup>b</sup> mA·cm <sup>−2</sup>	0.1 M KHCO <sub>3</sub>	81%	[61]
Zn Nanosheets	Electrochemical reduction	~24 h	−1.0	~8 <sup>b</sup> mA·cm <sup>−2</sup>	0.1 M KHCO <sub>3</sub>	90%	[62]
HP-Zn	Electrochemical reduction	8 h	−1.10	10 mA·cm <sup>−2</sup>	0.1 M KHCO <sub>3</sub>	91.3%	[63]
CTAB-Zn Nanosheets	Surfactant-modified Zn nanosheets	12 h	−1.10	13.1 mA·cm <sup>−2</sup>	0.5 M KHCO <sub>3</sub>	95.6%	[64]
OD-Zn-CTAB	Electrochemical reduction	14 h	−1.0	8.2 mA·cm <sup>−2</sup> (pcd)	0.1 M KHCO <sub>3</sub>	90%	[65]
Zn Nanosheets	alkali corrosion and electrochemical restructuring	14 h	−0.90	9.9 mA·cm <sup>−2</sup>	0.5 M KHCO <sub>3</sub>	92%	[66]

<sup>a</sup> This value is converted to RHE scale based on the information in the article. <sup>b</sup> This value is not mentioned in the article but derived from the graphical results.

In addition, compared to Zn foil, the FE and the rate of production of CO of the *h*-Zn were significantly improved. The highest CO Faraday efficiency of 85.4% was obtained at  $-0.95$  V<sub>RHE</sub> (Figure 4b). Stability is a key factor in the performance of a catalyst, which is one of the essential elements for commercial applications. Therefore, the same authors evaluated the catalyst performance of *h*-Zn for long-term operation and found that *h*-Zn exhibited stable electrolysis performance with a current density of around  $9.5$  mA·cm<sup>−2</sup> for 30 h, while the CO Faraday efficiency remained at 80% for  $-0.85$  V<sub>RHE</sub>. CO<sub>2</sub>RR activity and selectivity are strongly dependent on the crystal plane of the catalyst [50,60,67]. Woo et al. used density functional theory (DFT) calculations to analyze the origin of the catalytic selectivity derived from Zn crystal planes. Generally, the reduction of CO<sub>2</sub> to CO includes the following three equations (Equations (2)–(4)) [68].



When calculating the reduction of CO<sub>2</sub> on the (002) and (101) facets of Zn, the kinetic activity of the adsorption energy of the COOH\* (Equation (2)) and CO\* intermediates

(Equation (3)) for the CO's formation should be considered DFT calculations to demonstrate that the (101) facet was appropriate for the CO's production, due to its lower reduction potential for CO<sub>2</sub> reduction to CO and its higher energy barrier for HER than the (002) facet (Figure 4c,d) [50]. In other words, to promote the formation of CO on Zn catalysts, the surface of the Zn should be optimized and dominantly exposed with (101) facets to suppress HER. Similar conclusions were obtained in Zhang's work on the electroreduction of CO<sub>2</sub> using multilayer Zn nanosheet electrocatalysts [59]. In addition, Woo et al. proved that the product distribution of CO/H<sub>2</sub> can be controlled by experimentally designing the crystal plane ratio on the Zn electrode. This conclusion was also confirmed by Peng et al. [60]. The CO/H<sub>2</sub> ratio of the electroreduction of CO<sub>2</sub> to syngas can be adjusted within the range of 0.2~2.31 over Zn catalysts with different crystal ratios of Zn (002) and Zn (101) [60].

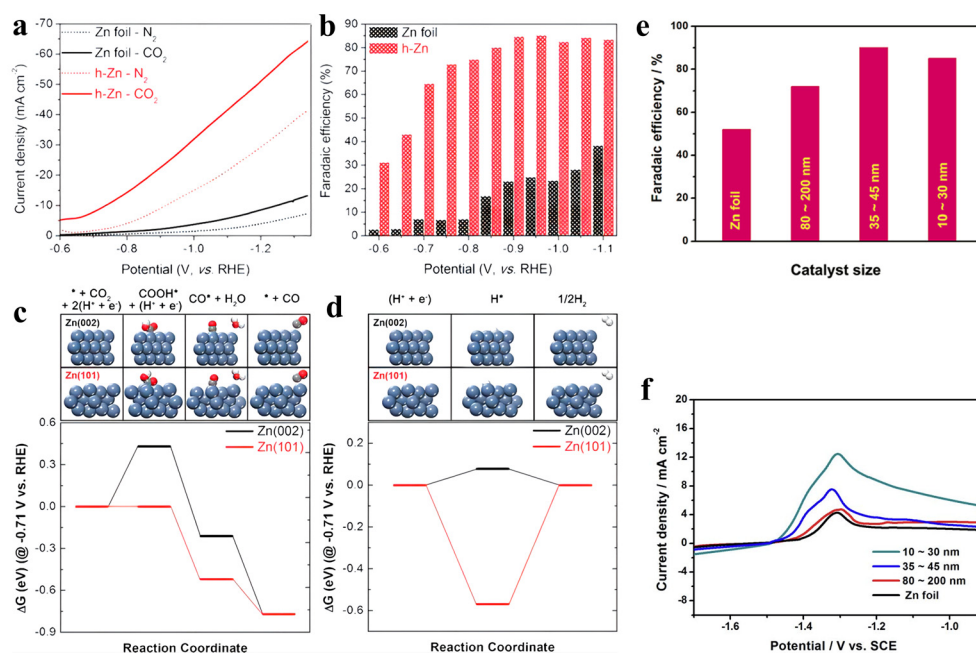


**Figure 4.** (a) LSV results in a N<sub>2</sub> (dotted line) or CO<sub>2</sub>-saturated (solid line) 0.5 M KHCO<sub>3</sub> electrolyte with a 50 mVs<sup>-1</sup> scan rate. (b) FE of CO at various constant potentials ranging from −0.6 to −1.1 V. (c) Free-energy diagrams for CO<sub>2</sub> reduction and (d) free-energy diagrams for HER on Zn (002) (black solid line) or Zn (101) (red solid line) At −0.71 V. Atomistic structures optimized for each step are shown on the top. Navy blue, gray, red, and white colors represent Zn, C, O, and H atoms, respectively [50]. Reproduced from Ref. [50] with permission. © 2023 WILEY-VCH Verlag GmbH & Co. KGaA, Weinheim. (e) Dependence of FE<sub>CO</sub> on the zinc catalyst size. (f) LSV scans (from −1.7 to −0.9 V) in Ar-saturated 0.1 M NaOH for Zn catalysts with different particle sizes [53]. Reproduced from Ref. [53] with permission from the Royal Society of Chemistry.

Another opinion is that the crystalline surface of Zn (100) favors the formation of CO [51]. DFT calculations indicated that, compared to the (002) facet of Zn, there were low-coordinated atoms in the (100) facet, thus resulting in an upward shift of the d-band center. Therefore, stronger binding of the \*COOH intermediate to the (100) facet favors the production of CO as compared to the (002) facet. In addition, Zn nanostructures have a high density of edge and corner sites. Corner sites tend to over-constrain CO\* in favor of HER, whereas the edge sites favor the CO<sub>2</sub>RR to CO. The superior performance of hexagonal Zn nanosheets with a 94.2% Faraday efficiency for CO at −0.96 V<sub>RHE</sub> was confirmed by the increase in the ECSA, the decrease in the work function, and the increase in the number of Zn (100) and edge atoms.

The reduction rate of CO<sub>2</sub> is proportional to the desorption rate of CO. The low desorption rate of CO contributes to the depressed kinetics of the CO<sub>2</sub> reduction reaction. Therefore, Luo et al. prepared a porous Zn electrode (P-Zn) using electrodeposition for the

CO<sub>2</sub>RR that obtained an excellent Faraday efficiency of 94.4% for CO and a large current density of 27 mA·cm<sup>-2</sup> at -0.95 V<sub>RHE</sub> in a CO<sub>2</sub>-saturated 0.5 M KHCO<sub>3</sub> solution [52]. Wang and co-workers prepared a three-dimensional (3D) hierarchically porous Zn (HP-Zn) with lots of hierarchical macroporous (~300 nm), interconnected nanopores (<100 nm), and nanopores (5–20 nm) using the hydrogen-mediated approach [63]. The abundance of mesopores in the electrode generated a large number of active areas. The interconnected pores provided a growth site for CO bubbles and an efficient transport path for large-scale CO<sub>2</sub> transport. This was due to the porous structure of HP-Zn that exhibited excellent performance during the reduction of CO<sub>2</sub> with the highest CO Faraday efficiency of 91.3% and a current density of 10.0 mA·cm<sup>-2</sup> at -1.1 V<sub>RHE</sub> that far exceeded that of ZnO NPs (73%) and Zn foil (39%). Moreover, the Tafel slope of the HP-Zn (78 mV·dec<sup>-1</sup>) was smaller than that of the ZnO NPs (98 mV·dec<sup>-1</sup>) and Zn foil (115 mV·dec<sup>-1</sup>), thus suggesting that the 3D structures could enhance the kinetics of the rate-determining step (RDS). In addition, the 3D structures can regulate the local pH near the electrode. When both the HER and CO<sub>2</sub>RR produce hydroxide ions (OH<sup>-</sup>), the mass transfer limitations of the 3D structures with complicated pores inhibit the neutralization of OH<sup>-</sup>, thereby leading to an increase in local pH. The high local pH suppresses the evolution of H<sub>2</sub>, which results in enhanced CO selectivity [52,69,70]. Apart from the electrode structure, the local pH value is taken in relation to the buffering strength of the electrolyte, the saturation of CO<sub>2</sub>, the diffusion coefficients of the substrates and products, and the stirring of the reactor [30].

The size of the Zn catalyst also has a significant effect on the Faraday efficiency for CO production. Zn catalysts with different particle sizes, such as Zn foil, 10–30 nm, 35–45 nm, and 80–200 nm Zn NPs, were applied in the CO<sub>2</sub>RR at the potential of -1.6 V in a 0.5 M NaCl solution (Figure 4e). The Faraday efficiency of CO increased in the following ascending order: Zn foil < 10–30 nm < 80–200 nm < 35–45 nm Zn NPs. The highest CO Faraday efficiency of 91% was produced for the Zn catalyst obtained from the reduction of 35–45 nm ZnO nanoparticles. Furthermore, nanoscale metal catalysts are thought to be able to stabilize adsorption intermediates, thus leading to the efficient conversion of CO<sub>2</sub>. In order to investigate the effect of particle size on the adsorption of intermediates, Jia et al. [53] studied the behavior of different Zn electrodes in an Ar-saturated 0.1 M NaOH solution using linear voltammetry to examine the adsorption of hydroxyl radicals (as a representative of CO<sub>2</sub> intermediates) (Figure 4f). They found that, as the particle size of the particles increased, the onset potential for the adsorption of hydroxyls was positively shifted, thereby showing that the smaller particles have a higher hydroxyl binding energy. This means that the smallest Zn nanoparticles (10–30 nm) could effectively immobilize the CO<sub>2</sub><sup>•-</sup> intermediate [62,71]. However, the smallest Zn nanoparticles (10–30 nm) were not optimal for reducing CO<sub>2</sub>. The reason may be that the affinity is too strong to hinder the following conversion of the intermediate and release the product. The maximum Faraday efficiency of CO obtained for Zn nanoparticles (35–45 nm) could be ascribed to their optimal binding strength to the intermediate during the reduction of CO<sub>2</sub> [53]. Moreover, to explore the size-dependent activity and selectivity for CO<sub>2</sub>RRs of Zn, size-controlled Zn nanoparticles were synthesized using inverse micelle encapsulation in a PS-P2VP dimer (Figure 5a–d) [58]. According to the results, the variation trends of activity and selectivity for CO<sub>2</sub>RRs could be separated into three different NP size regimes: (i) <3 nm—high activity with low CO selectivity; (ii) 3–5 nm—high activity and similar CO selectivity compared to bulk Zn; and (iii) >5 nm—decreased activity with constant CO selectivity (Figure 5e,f). This is consistent with the DFT results on Au NPs [72]. It can be inferred that a high H coverage is expected on small nanoparticles due to the enhanced ratio of low coordination sites, under which the condition of the binding of reaction intermediates, such as COOH\*, is weakened, resulting in lower CO production than H<sub>2</sub>. The authors also suggested that the Zn-based catalyst was not completely reduced to metallic zinc during the CO<sub>2</sub>RR, even at strong negative potentials. The remaining metal oxides can affect the activity and selectivity of the catalyst [73,74]. They concluded that the unique selectivity trends observed could not be attributed exclusively to the structural changes on the surface

of large NPs or their nanostructures. Other factors such as local pH, the presence of  $Zn^{2+}$ , and adsorbed ions should be taken into account. In addition, their work showed that the selectivity of the  $CO_2RR$  can also be tuned by stabilizing cationic Zn species under the reaction conditions.

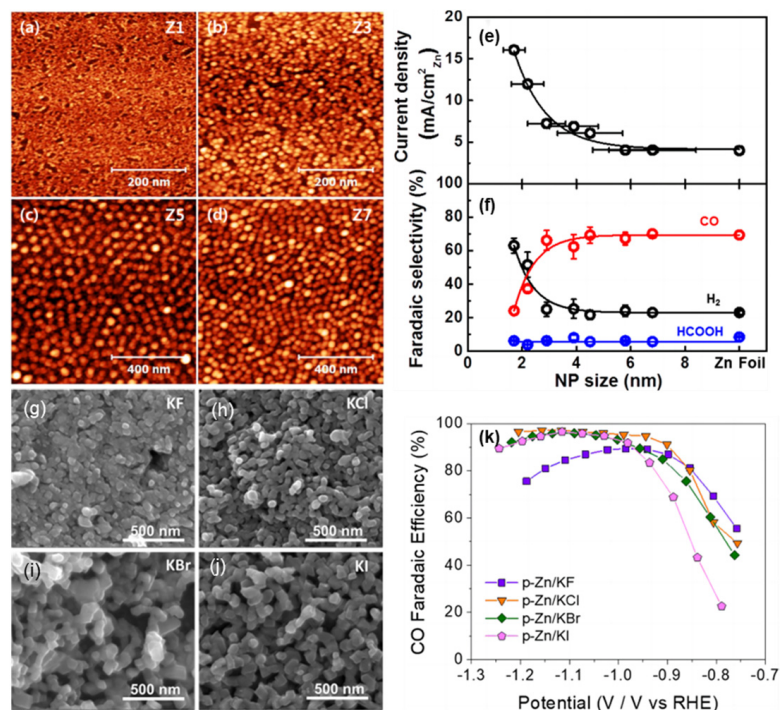


**Figure 5.** (a–d) AFM images of Zn NP samples prepared via inverse micelle encapsulation and supported on  $SiO_2/Si(111)$ .  $Zn_1$  ( $1.7 \pm 0.4$  nm),  $Zn_3$  ( $2.9 \pm 0.7$  nm),  $Zn_5$  ( $4.5 \pm 1.2$  nm), and  $Zn_7$  ( $6.8 \pm 1.6$  nm). (e) Current densities of  $CO_2RR$ s over Zn NPs. (f) Faradaic selectivity toward  $H_2$ , CO, and HCOOH measured at  $-1.1 V_{RHE}$  in  $0.1 M KHCO_3$  as a function of the Zn NP size [58]. Reproduced with permission from Ref. [58]. Copyright © 2023, American Chemical Society. (g–j) SEM images of p-Zn/KF, p-Zn/KCl, p-Zn/KBr and p-Zn/KI pre- $CO_2RR$ . (k) CO Faradaic efficiency of Zn-based electrocatalysts [71]. Reproduced with permission from Ref. [71]. © 2023 Elsevier B.V. All rights reserved.

Zn is susceptible to oxidation, while halide anions are highly electronegative and nucleophilic. Therefore, halides can adsorb on the surface of Zn nanostructures or halide anions to interact on the surface of zinc oxide. These may strongly affect the nanostructure, morphology, or chemical state of the Zn-based catalysts, which are believed to be important factors in determining the activity of CO reduction [75,76]. Hwang et al. systematically studied the influence of halides ( $F^-$ ,  $Cl^-$ ,  $Br^-$ , or  $I^-$ ) on nanoporous Zn electrocatalysts [76] (Figure 5g–k). Zn-catalysts exhibited good  $CO_2RR$  performance with a Faraday efficiency of up to 97% for CO in the presence of halides (Figure 5k). The increase in adsorption strength from  $F^-$  to  $I^-$  could change the morphology and roughness of the nanostructure of porous Zn, as well as the formation of higher Zn oxidation states. These changes promoted the protonation of  $CO_2$ , stabilized the adsorbed intermediates, and enhanced the  $CO_2RR$ . The pH values increased in the following ascending order: KI (2.53) < KBr (2.96) < KCl (3.91) < KF (6.8). It is supposed that low pH (high proton concentration) would be favorable for HER. However, researchers found that the p-Zn/KF catalyst was the least effective in inhibiting HER. It is possible that the weaker adsorption of  $F^-$  leads to a rougher and denser morphology of p-Zn/KF and fewer oxidized Zn species, which results in a slower rate of desorption of CO and a lower inhibitory efficiency of HER.

Surface modification is an effective way to further improve the catalytic performance of materials for  $CO_2RR$ s [77–80]. Recently, Wang et al. [64] reported that modified Zn

nanosheets (NSs) produced using different amounts of cetyltrimethylammonium bromide (CTAB). It was observed that the CTAB-modified Zn NSs showed much higher activity than the parent Zn NSs. Among them, Zn NSs-1.6 had the best catalytic activity with a high Faraday efficiency of 95.6% for CO and a current density of  $13.1 \text{ mA}\cdot\text{cm}^{-2}$  at  $-1.1 \text{ V}_{\text{RHE}}$  (Figure 6a,b). Meanwhile, the Faraday efficiency of CO is greater than 90%, over a wide range of potentials ( $-0.9$ – $1.1 \text{ V}$ ) (Figure 6b). Later, it was found that the amount of CTAB modification affected the partial current density of CO (Figure 6c). Zn NSs-1.6 exhibited excellent  $j_{\text{CO}}$  within the range of  $0.07$ – $12.5 \text{ mA}\cdot\text{cm}^{-2}$  with a voltage change lying within the range of  $0.6$ – $1.1 \text{ V}$ . This indicates that the electroreduction of  $\text{CO}_2$  is more active after surfactant modification. Simultaneously, the Zn electrode modified by CTAB also showed long-term durability at  $-1.0 \text{ V}_{\text{RHE}}$  over 12 h without obvious attenuation in terms of the Faraday efficiency ( $>90\%$ ) for CO and current density ( $\sim 9.1 \text{ mA}\cdot\text{cm}^{-2}$ ) (Figure 6d). Furthermore, the minimum Tafel slope values obtained on Zn NSs-1.6 (Figure 6e) indicate that the reaction kinetics of Zn NSs-1.6 and CTAB were favorable compared to pure Zn NSs. Moreover, the more negative adsorption potential of  $\text{OH}^-$  on Zn NSs-1.6 (Figure 6f) indicates a stronger adsorption effect. Furthermore, after modification of the CTAB, the Zn NS electrode stabilized the  $\text{CO}_2^{\bullet-}$  intermediate, leading to an increase in the activity of  $\text{CO}_2\text{RRs}$  to CO. The same authors concluded that the positively charged groups of CTAB prevented the proton from approaching the surface of electrode, and, therefore, the reduction of  $\text{H}^+$  was impeded. The hydrophobic long chains of CTAB offered channels for the diffusion of  $\text{CO}_2$  to the surface of the electrode.

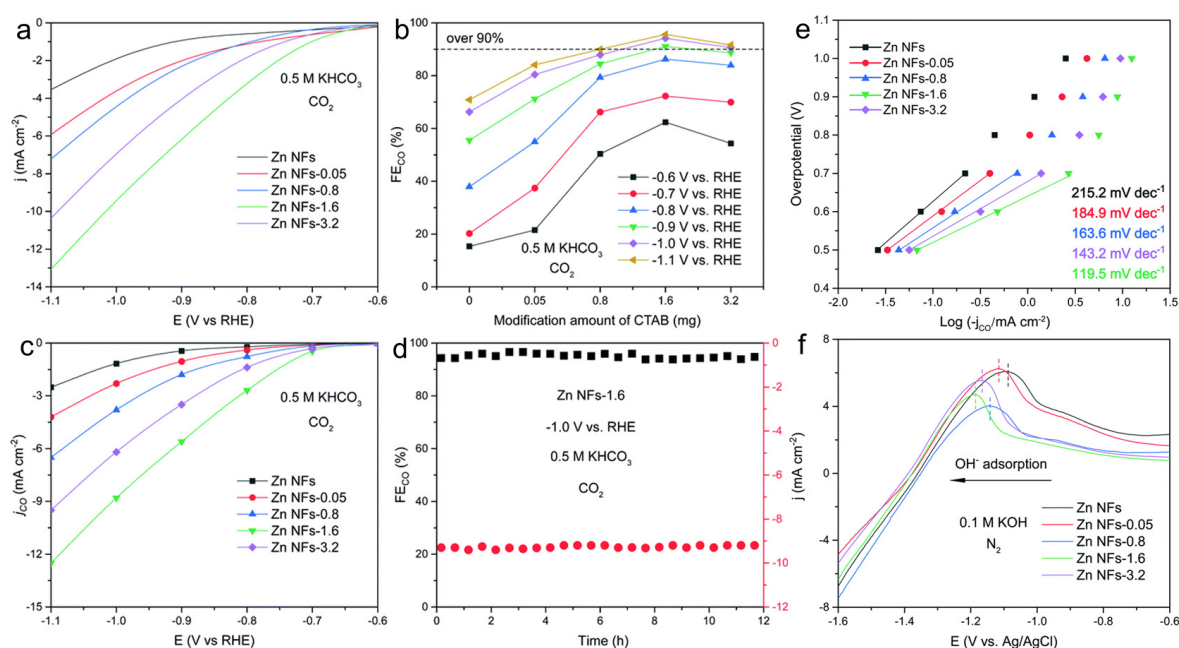


**Figure 6.** (a) LSV curves of Zn NSs modified with CTAB (0–3.2 mg). (b)  $\text{FE}_{\text{CO}}$  of Zn modified with CTAB (0–3.2 mg). (c)  $j_{\text{CO}}$  for Zn NSs and CTAB-modified Zn NSs. (d) Durability of Zn NSs-1.6 measured in potassium bicarbonate electrolyte (0.5 M). (e) Tafel slopes of Zn NSs modified with CTAB (0–3.2 mg). (f) Single oxidative LSV curves of samples measured in potassium hydroxide solution (0.1 M) [64]. Reproduced from Ref. [64] with permission from the Royal Society of Chemistry.

### 3.1.2. Zinc Monomer Catalyst for $\text{CO}_2$ Reduction to Formate

Formate is considered a suitable material for fuel cells and a viable pathway for hydrogen storage [81]. Metal catalysts, such as Pb and Hg, are considered to be the most promising options for the effective reduction of  $\text{CO}_2$  to formate [17]. However, most of them are extremely toxic and/or expensive. Furthermore, they do not exhibit simultaneous high Faraday efficiencies and high current densities. The development of low-cost, non-toxic, highly selective, stable, and high current density electrocatalysts for

the conversion of CO<sub>2</sub> to formate is essential. According to Purkait's work [82], Zn powder enhanced the conversion of CO<sub>2</sub> to HCOOH with a maximum Faraday efficiency of 78.46%. However, the stability was very short at only 10 min. Recently, Zhang et al. demonstrated that CO<sub>2</sub> could be selectively converted to formate over a zinc catalyst with a layer of nanoparticles (RAD-Zn) [81]. The maximum Faraday efficiency of the RAD-Zn electrode for formate was 87.1% at  $-1.93 V_{RHE}$  with a formate partial current density of  $12.8 \text{ mA}\cdot\text{cm}^{-2}$ . Furthermore, the catalytic activity was 17 times that of the zinc foil, while the Faraday efficiency of the formate was 8 times that of the zinc foil. In addition, the authors found no significant deterioration in the Faraday efficiency and current density after 14 h of continuous electrolysis. They attributed the improved catalytic performance of the RAD-Zn to the formation of polycrystalline, catalytically active crystal surfaces and especially to the Zn surface structure during the reduction of polycrystalline ZnO [81]. Since Zn is polycrystalline, it is difficult to determine the active surface for the selective generation of formic acid using the electrochemical reduction of CO<sub>2</sub>. To explore the relationship between the active crystal surface and the activity of the catalyst, an anodized Zn electrode with adjustable exposure of facet that was synthesized by varying the anodization voltage was used in CO<sub>2</sub>RRs [83]. X-ray diffraction (XRD) characterization demonstrated that the main crystallographic orientations of Zn (001) and Zn (101) were obtained at the oxidation voltages of 8 V and 14 V, respectively. Haruyama et al. [83] obtained the highest formate Faraday efficiency of over 60% with Zn electrodes anodized at 14 V at the applied potential of  $-1.19 V_{RHE}$ . Their experimental results suggest that Zn (101) may be highly active during the formation of formate.

### 3.2. Zn-Based Bimetallic Materials

In order to improve the performance of Zn catalysts for CO<sub>2</sub>RRs, not only the nanostructures of Zn, engineering of Zn, and modification of Zn electrodes have been proposed, but also the introduction of secondary metals to create bimetallic structural motifs has also been put forward [84]. Bimetals are attractive CO<sub>2</sub>RR materials, because they provide multiple binding sites for reaction intermediates. Meanwhile, altering their structure, composition, and morphology could be better for catalytic performance [45,85–90]. For achieving the efficient electroreduction of CO<sub>2</sub>, a series of Zn-based bimetallic materials such as Zn–Cu, Zn–Ag, Zn–Pt, and Zn–Sn were prepared and employed for the reduction of CO<sub>2</sub>. Their catalytic performances are listed in Table 3.

**Table 3.** Summarized CO<sub>2</sub>RR activity of Zn-based bimetallic materials.

Electrocatalyst	Durability	Potential	Current Density	Electrolyte	Main Product	FE	Ref
Cu <sub>9</sub> Zn <sub>1</sub> /PTFE	7 h	$-0.76 V_{RHE}$	$93 \text{ mA}\cdot\text{cm}^{-2}$	1M KOH	C <sub>2</sub> H <sub>5</sub> OH	~25%	[38]
Cu <sub>70</sub> Zn <sub>30</sub> NPs	1 h	$-1.35 V_{RHE}$	$\sim 38^a \text{ mA}\cdot\text{cm}^{-2}$ (pcd <sup>b</sup> )	0.1 M KHCO <sub>3</sub>	CH <sub>4</sub>	70.2%	[84]
Zn–Cu (5s)	20 h	$-0.96 V_{RHE}$	$3.09 \text{ mA}\cdot\text{cm}^{-2}$ (pcd)	0.1 M KHCO <sub>3</sub>	CO	97%	[91]
CuZn <sub>0.4</sub>	4 h	$-1.0 V_{RHE}$	$4.3 \text{ mA}\cdot\text{cm}^{-2}$ (pcd)	0.1 M KHCO <sub>3</sub>	CO	70%	[92]
Phase-separated Cu–Zn NW	15 h	$-1.0 V_{RHE}$	$\sim 16 \text{ mA}\cdot\text{cm}^{-2}$ (pcd)	0.1 M KHCO <sub>3</sub>	CO	94%	[93]
Core-shell Cu–Zn NW	-	$-1.0 V_{RHE}$	$\sim 10 \text{ mA}\cdot\text{cm}^{-2}$ (pcd)	0.1 M KHCO <sub>3</sub>	CO	82%	[93]
Cu/Zn	4 h	$-1.6 V_{RHE}$	$0.7 \text{ mA}\cdot\text{cm}^{-2}$ (pcd)	0.5 M KCl	CH <sub>4</sub>	52%	[94]
Cu <sub>5</sub> Zn <sub>8</sub>	-	$-1.0 V_{Ag/AgCl}$	-	0.1 M KHCO <sub>3</sub>	HCOOH	71.1%	[95]
Zn–Cu	18 h	$-1.0 V_{RHE}$	$\sim 3.1 \text{ mA}\cdot\text{cm}^{-2}$	0.5 M KHCO <sub>3</sub>	CO HCOOH	48.7% <sup>a</sup> 25.3% <sup>a</sup>	[96]
Zn <sub>75</sub> Cu <sub>25</sub> Alloy	>9 h	$-0.9 V_{RHE}$	$\sim 13 \text{ mA}\cdot\text{cm}^{-2}$ (pcd)	0.1 M Cs <sub>2</sub> CO <sub>3</sub>	Syngas	94% <sup>a</sup>	[97]
Zn–Bi	7 h	$-0.8 V_{RHE}$	$3.5^a \text{ mA}\cdot\text{cm}^{-2}$	0.5 M NaHCO <sub>3</sub>	HCOOH	94%	[98]
Zn–In	24 h	$-1.2 V_{RHE}$	$22 \text{ mA}\cdot\text{cm}^{-2}$ (pcd)	0.5 M KHCO <sub>3</sub>	HCOOH	95%	[99]
Zn–Sn	12 h	$-1.06 V_{RHE}$	$9.95 \text{ mA}\cdot\text{cm}^{-2}$ (pcd)	0.5 M KHCO <sub>3</sub>	HCOOH	94%	[100]
Pd–Zn/CB	-	$-0.1 V_{RHE}$	-	0.1 M KHCO <sub>3</sub>	HCOOH	99.4%	[101]
Pd–Zn–GCN	17 h	$-0.90 V_{RHE}$	$4.4 \text{ mA}\cdot\text{cm}^{-2}$ (pcd)	0.1 M KCl	CO	93.6%	[102]
Pt <sub>x</sub> Zn/C	16 h	$-0.90 V_{RHE}$	-	0.1 M NaHCO <sub>3</sub>	CH <sub>3</sub> OH	81.4%	[103]
Zn–Sb	6 h	$-1.0 V_{RHE}$	$7.6 \text{ mA}\cdot\text{cm}^{-2}$ (pcd)	0.5 M KHCO <sub>3</sub>	HCOOH	92%	[104]
Zn–Ni	~11 h	$-0.9 V_{RHE}$	$8.25 \text{ mA}\cdot\text{cm}^{-2}$ (pcd) <sup>a</sup>	0.1 M KHCO <sub>3</sub>	HCOOH	36%	[105]

Table 3. Cont.

Electrocatalyst	Durability	Potential	Current Density	Electrolyte	Main Product	FE	Ref
Zn <sub>3</sub> Sn <sub>2</sub>	12 h	−1.1 V <sub>RHE</sub>	26.0 mA·cm <sup>−2</sup> (pcd)	0.5 M KHCO <sub>3</sub>	HCOOH	96.7%	[106]
3-Cu–Zn	1 h	−0.91V <sub>RHE</sub>	10.16 mA·cm <sup>−2</sup>	0.5 M KHCO <sub>3</sub>	HCOOH CO	21.6% 30.7%	[107]
Zn–Cu@Cu	12 h	−1.25 V <sub>RHE</sub>	21.4 mA·cm <sup>−2</sup> (pcd)	0.5 M NaHCO <sub>3</sub>	HCOOH	48.6%	[108]
s-Cu <sub>1</sub> Zn <sub>3</sub> O <sub>x</sub>	50 h	−2.16 V <sub>RHE</sub>	93 <sup>a</sup> mA·cm <sup>−2</sup> (pcd)	1 M KOH	CH <sub>4</sub>	23% <sup>a</sup>	[109]
Cu–Zn alloy	15 h	−1.1 V <sub>RHE</sub>	6.1 mA·cm <sup>−2</sup>	0.1 M KHCO <sub>3</sub>	C <sub>2</sub> H <sub>4</sub>	33.3%	[110]
HMMPCu <sub>5</sub> Zn <sub>8</sub>	11 h	−0.8 V <sub>RHE</sub>	3.6 mA·cm <sup>−2</sup>	0.1 M KHCO <sub>3</sub>	C <sub>2</sub> H <sub>5</sub> OH	46.6%	[111]
Cu <sub>75</sub> Zn <sub>25</sub> –C	7 h	−1.0 V <sub>RHE</sub>	6.7 mA·cm <sup>−2</sup>	0.1 M KHCO <sub>3</sub>	C <sub>2</sub> H <sub>4</sub>	15%	[112]
OD-Cu <sub>75</sub> Zn <sub>25</sub> (cubes)	-	−1.1 V <sub>RHE</sub>	-	0.1 M KHCO <sub>3</sub>	C <sub>2</sub> H <sub>4</sub> C <sub>2</sub> H <sub>5</sub> OH	41.1% 16.1%	[113]
Zn <sub>0.87</sub> Ag <sub>0.13</sub> GDE	100 h	−1.15 V <sub>RHE</sub>	100 mA·cm <sup>−2</sup>	1M KCl	CO	96%	[114]
Ag–Zn	-	−1.2 V <sub>RHE</sub>	-	0.1 M KHCO <sub>3</sub>	CO	63%	[115]
AgNN@Zn <sub>15</sub>	12 h	−0.86 V <sub>RHE</sub>	-	0.5 M KHCO <sub>3</sub>	CO	91.05%	[116]
CP/PPy/Zn/Ag	-	−1.3V <sub>RHE</sub>	8.6 mA·cm <sup>−2</sup> (pcd)	0.1 M KHCO <sub>3</sub>	CO	~70%	[117]
Ag-alloyed Zn	40 h	−0.9 V <sub>RHE</sub>	21 mA·cm <sup>−2</sup> (pcd)	0.1 M CsHCO <sub>3</sub>	CO	97%	[118]
Zn <sub>94</sub> Cu <sub>6</sub>	36 h	−0.95 V <sub>RHE</sub>	5 mA·cm <sup>−2</sup> <sup>a</sup>	0.5 M KHCO <sub>3</sub>	CO	90%	[119]
Ag–Zn	40 h	−1.0 V <sub>RHE</sub>	2.97 mA·cm <sup>−2</sup> (pcd)	0.1 M KHCO <sub>3</sub>	CO	84.2%	[120]
Cu <sub>2</sub> O/ZnO (1:1)	5 h	−1.3V <sub>Ag/AgCl</sub>	10.64 mA·cm <sup>−2</sup>	0.5 M KHCO <sub>3</sub>	CH <sub>3</sub> OH	17.7%	[121]
SnO <sub>2</sub> /ZnO	-	−1.3 V <sub>RHE</sub>	24.9 mA·cm <sup>−2</sup> (pcd)	0.5 M KHCO <sub>3</sub>	HCOOH	98%	[122]
Cu <sub>4</sub> Zn	5 h	−1.05 V <sub>RHE</sub>	8.2 mA·cm <sup>−2</sup>	0.1 M KHCO <sub>3</sub>	C <sub>2</sub> H <sub>5</sub> OH	29.1%	[123]
Cu <sub>2</sub> O/ZnO-GDEs	20 h	-	10 mA·cm <sup>−2</sup>	0.5 M KHCO <sub>3</sub>	CH <sub>3</sub> OH	27.7 <sup>a</sup>	[124]
CuO/ZnO/C	75 h	−0.75 V <sub>RHE</sub>	367 mA·cm <sup>−2</sup>	1 M KOH	C <sub>2</sub> H <sub>4</sub>	50.9%	[125]
GuZn <sub>20</sub> /NGN	24 h	−0.8 V <sub>RHE</sub>	3.95 mA·cm <sup>−2</sup>	0.1 M KHCO <sub>3</sub>	C <sub>2</sub> H <sub>5</sub> OH n-C <sub>3</sub> H <sub>7</sub> OH	34.25% 12.38%	[126]
Cu/ZnO	10 h	−0.73 V <sub>RHE</sub>	466 mA·cm <sup>−2</sup> (pcd)	1 M KOH	C <sub>2</sub> <sup>+</sup>	78%	[127]
CuO–ZnO <sub>10</sub>	12 h	−0.8 V <sub>RHE</sub>	3.78 mA·cm <sup>−2</sup>	0.1 M KHCO <sub>3</sub>	C <sub>2</sub> H <sub>5</sub> OH	22.27%	[128]

<sup>a</sup> This value is not mentioned in the article but derived from the graphical results. <sup>b</sup> pcd represents partial current density.

### 3.2.1. Zn–Cu Bimetallic Materials

In recent years, with the discovery of multi-component systems and their prominent role in electrocatalysis, the interaction between Zn and Cu or their compounds has attracted the attention of researchers. Cu–Zn bimetallic catalysts have been suggested as an effective way to enhance the catalytic performance of CO<sub>2</sub>RRs [129] and are of interest due to their low cost and environment friendliness. High selectivity for the generation of CO from CO<sub>2</sub>RR has been achieved on Zn–Cu bimetallic materials. For instance, Hahn et al. [91] employed a galvanic exchange procedure to prepare Zn–Cu bimetallic electrocatalysts with different Zn contents for the reduction reaction of CO<sub>2</sub> to CO. They found that the intrinsic activity of Zn-rich Zn–Cu towards the formation of CO was superior to that of pure Zn and Cu. DFT calculations indicated that the bimetallic effect contributes to the overall reaction rate of the production of CO by stabilizing the carboxylate (COOH\*) intermediate. Zeng et al. [92] prepared Cu–Zn bimetallic catalysts (CuZn<sub>0.1</sub>, CuZn<sub>0.25</sub>, CuZn<sub>0.4</sub>, and CuZn<sub>0.5</sub>) using a microwave-assisted solvothermal method and applied them to CO<sub>2</sub>RRs. The average Faraday efficiency of the CuZn<sub>0.4</sub> catalyst for the generation of CO and HCOOH was 70% and 28%, respectively. They suggested that, at the bimetallic electrode, the active site of ZnO is selective for the generation of CO, whereas the high conductivity of Cu favors the transfer of the electron. Luo et al. [93] prepared two types of Cu–Zn bimetallic catalysts with phase-separated and core-shell structures (Figure 7a), and investigated their performance for CO<sub>2</sub>RRs. The distributions of metallic elements in different structures are shown in Figure 7b,c. The phase-separated sample showed higher CO<sub>2</sub>RR activity than the core-shell sample because of its larger positive onset potential and current density in a CO<sub>2</sub>-saturated 0.1 M KHCO<sub>3</sub> solution (Figure 7d), which exhibited a 94% CO Faraday efficiency (Figure 7e) with a 16 mA·cm<sup>−2</sup> current density at −1.0 V<sub>RHE</sub>. After 20 min of an electrocatalytic CO<sub>2</sub>RR, they characterized the Cu–Zn samples using transmission electron microscopy (TEM), high-resolution TEM (HR-TEM), and energy dispersive X-ray spectroscopy (EDX) mappings (Figure 7f–k). They found that, after electrolysis, a thin layer of Zn was produced on the core-shell Cu–Zn bimetallic sample, thereby indicating a

redistribution of elements on the surface (Figure 7). According to their DFT calculations, the phenomenon could be due to the strong tension of the  $^*COOH$  intermediate on the Zn in the core-shell sample. In addition, DFT calculations showed enhanced stability of the  $^*COOH$  intermediate due to the lower energy barrier over the phase-separated Cu–Zn nanowires (NW) sample, thus confirming its higher activity of  $CO_2RR$ . Nanoporous Cu–Zn catalysts prepared using annealing and reducing commercial Cu–Zn alloy films showed four and six times higher Faraday efficiencies for the generation of CO and HCOOH, respectively, than untreated Cu–Zn films [96]. Miyauchi's group [95] synthesized Cu–Zn alloy materials using a vacuum sealing method. The optimized  $Cu_5Zn_8$  alloy exhibited Faraday efficiencies of 71.1% for the generation of formic acid at  $-1.0 V_{Ag/AgCl}$  and 79.1% for the  $CO_2RR$  under ultraviolet light.

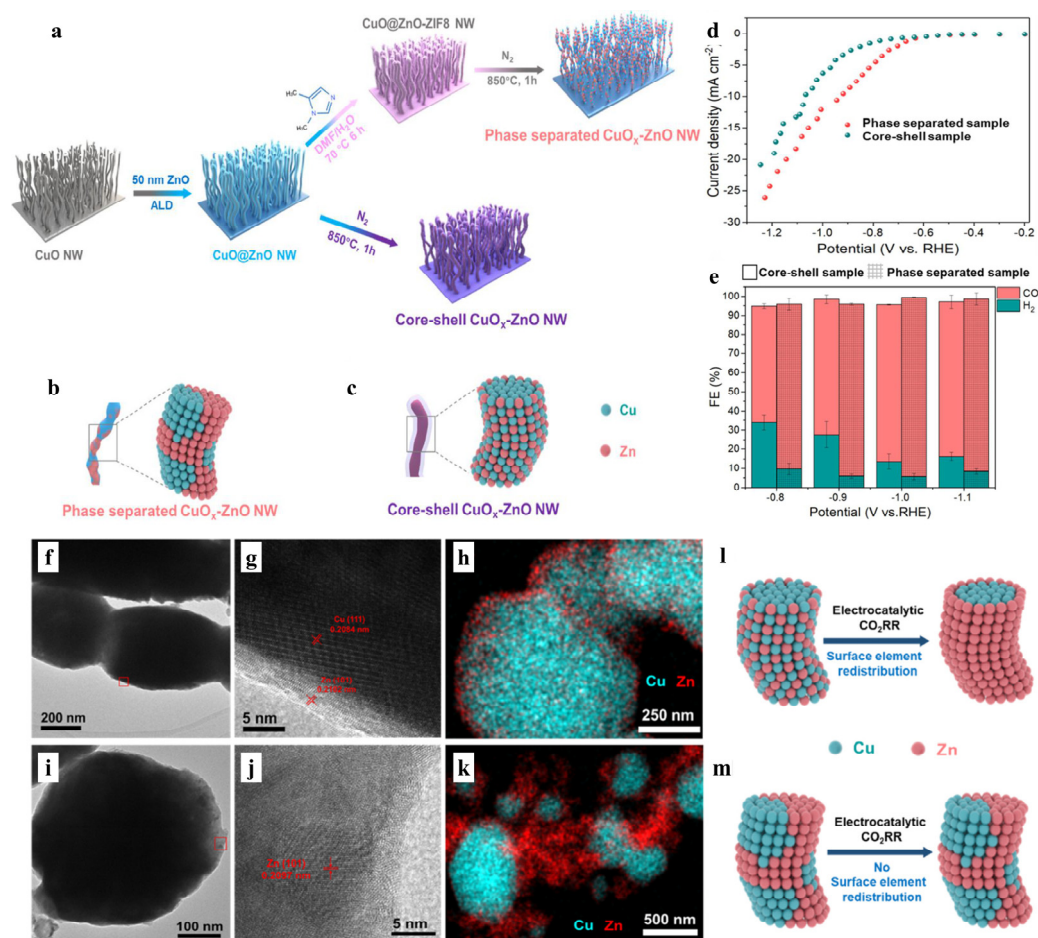


**Figure 7.** (a) Illustration of the synthesis process of phase-separated and core-shell  $CuO_x-ZnO$  NWs. (b,c) Schematic diagrams of phase-separated and core-shell samples in microscale (only metal elements are shown for a simplified and clarified illustration). Electrochemical  $CO_2$  reduction performance. (d) Linear sweep voltammetry curves of phase-separated and core-shell samples in  $CO_2$ -saturated 0.1 M  $KHCO_3$  solution. (e) FE of main products of core-shell and phase-separated samples. (f) Low resolution TEM image of the core-shell sample after 20 min electrocatalytic  $CO_2RR$ , (g) HR-TEM image of the red square part in (f). (h) EDX mapping of the core-shell sample. (i) TEM image of the phase-separated sample after 20 min electrocatalytic  $CO_2RR$ . (j) HR-TEM image of the red square part in (i). (k) EDX mapping of the phase-separated sample. (l) Element redistribution of core-shell and (m) phase-separated samples [93]. Reproduced from Ref. [93] with permission. Copyright © 2023, American Chemical Society.

These works show that the main product generated by the  $CO_2RR$  over Cu–Zn catalysts is either CO or HCOOH, which may be due to the lower Cu content in Zn-rich

$\text{Cu}_x\text{Zn}_y$ , thereby resulting in lower adsorption energy for both the surface  $^*\text{CO}_2$  and the  $^*\text{CO}$  species [47,110,130]. Generally speaking, product selectivity for  $\text{CO}_2$  reduction is determined by the strength of the binding of  $^*\text{CO}$  and  $^*\text{H}$  adsorbed on the metal surface [84]. Bulk copper polycrystalline electrodes exhibit moderate binding energy for adsorbed  $^*\text{CO}$ , whereas the hydrogenation of this  $^*\text{CO}$  species can produce  $\text{CH}_4$  [131]. However, for the polycrystalline Zn electrode, the binding strength of the adsorbed  $^*\text{CO}$  is relatively weak, thus resulting in the production of CO without further reaction [110,123]. Therefore, it is possible to produce  $\text{CH}_4$  as the main reduction product on a Cu–Zn electrode. For instance, hierarchically structured Zn-coated Cu electrodes that were synthesized using electrodeposition exhibited a Faraday efficiency of up to 52% for  $\text{CH}_4$ , which far exceeded that for bare Cu (23%) [94]. Cu–Zn nanocomposites (s- $\text{Cu}_1\text{Zn}_3\text{O}_x$ , and s- $\text{Cu}_5\text{Zn}_1\text{O}_x$ ) were prepared using a sputtering route and achieved around 23% FE for  $\text{CH}_4$  at  $-2.16 \text{ V}_{\text{RHE}}$  on s- $\text{Cu}_5\text{Zn}_1\text{O}_x$  [109]. Well-defined 5 nm  $\text{Cu}_{100-x}\text{Zn}_x$  ( $x = 10, 30, \text{ and } 50$ ) NPs that were synthesized using the inverse micelle encapsulation method exhibited an enhanced Faraday efficiency for  $\text{CH}_4$  (70.2%) compared to that of pure Cu NPs [84]. Chen et al. [132] demonstrated that the generation of  $\text{CH}_4$  is mainly dependent on the coordination number of Cu sites. Cu electrocatalysts with a low coordination number inhibited the C–C coupling involved in the  $\text{C}_{2+}$  products and enhanced the  $\text{C}_{1+}$  products.

Zn nanomaterials are known to be highly selective for CO, whereas Cu nanostructures can convert  $\text{CO}^*$  intermediates into hydrocarbon products [110]. Therefore, the electrochemical reduction of  $\text{CO}_2$  on Cu–Zn bimetallic nanomaterials is expected to generate hydrocarbons using a “relay catalysis” approach [47,133]. More specifically, the intermediates of  $\text{CO}^*$  are initially formed at the Zn sites, which then migrate to the adjacent Cu sites, where they can evolve further into hydrocarbon products [110]. Recent studies have shown that the electroreduction of  $\text{CO}_2$  on Cu–Zn catalysts favors the generation of  $\text{C}_{2+}$  products. For example, a series of oxide-derived phase segregation  $\text{Cu}_x\text{Zn}$  catalysts (Cu,  $\text{Cu}_{10}\text{Zn}$ ,  $\text{Cu}_4\text{Zn}$ , and  $\text{Cu}_2\text{Zn}$ ) with different Zn contents were prepared using electrodeposition. The catalysts exhibited distinct selectivity towards ethanol and ethylene [123]. Yeo et al. found that the selectivity of ethanol and ethylene could be altered by tuning the content of Zn. A maximum  $\text{C}_2\text{H}_5\text{OH}$  Faraday efficiency of 29.1% was obtained on  $\text{Cu}_4\text{Zn}$  with a current density of  $8.2 \text{ mA}\cdot\text{cm}^{-2}$  at  $-1.05 \text{ V}_{\text{RHE}}$ . A Raman activity pattern belonging to CO, adsorbed on Cu sites, was recorded during the production of ethanol, while no vibrations related to CO were observed on Zn, thus suggesting a further reduction of CO to ethanol on Cu sites. The authors demonstrated the spillover of CO from Zn to Cu sites, which increased the content of CO on the Cu site, thus further reducing it to  $^*\text{CHO}$  or  $^*\text{CH}$ . In addition,  $^*\text{CO}$  on the Zn sites with weak adsorption energy could enter the bond between the Cu site and the  $^*\text{CH}_2$  to generate  $^*\text{COCH}_2$ , which was further reduced to  $\text{C}_2\text{H}_5\text{OH}$  (Figure 8a) [123]. Bunyarat et al. [112] used a conductive porous carbon-loaded Cu–Zn bimetallic electrocatalyst ( $\text{Cu}_{90}\text{Zn}_{10}\text{-C}$ ,  $\text{Cu}_{75}\text{Zn}_{25}\text{-C}$ , and  $\text{Cu}_{50}\text{Zn}_{50}\text{-C}$ ) consisting of a mixed phase and alloy for  $\text{CO}_2\text{RR}$ s. They found that the variation in the distribution of Cu–Zn had a significant effect on the Faraday efficiency and current density of the  $\text{C}_2$  product during the  $\text{CO}_2\text{RR}$ . The highest Faraday efficiency of 23% was achieved for  $\text{C}_2$  products ( $\text{C}_2\text{H}_5\text{OH}$  and  $\text{C}_2\text{H}_4$ ) on the  $\text{Cu}_{75}\text{Zn}_{25}$  alloy, which was four times that of the Cu electrode and far superior to Cu–Zn catalysts with separated phases. DFT calculations showed that the Zn in the Cu–Zn alloy not only generated CO locally, but also affected the electronic structure of the Cu sites, thus contributing to CO–CO coupling and leading to enhanced  $\text{C}_2$  production [112]. Du et al. reported that homogeneous Cu–Zn alloy catalysts prepared using laser ablation in liquid showed good selectivity for  $\text{C}_2\text{H}_4$  in  $\text{CO}_2\text{RR}$ s [110] with a Faraday efficiency of 33.3%, which was more than twice as high as that of Cu NPs at  $-1.1 \text{ V}_{\text{RHE}}$  in a  $\text{CO}_2$ -saturated 0.1 M  $\text{KHCO}_3$  aqueous electrolyte. The Cu–Zn alloy showed a stable total current density, FE for  $\text{C}_2\text{H}_4$ , and CO for 15 h of electrolysis. The authors suggested that the dimerization [134] and protonation of  $\text{CO}^*$  species transferred from the Zn sites to the Cu sites promoted the production of  $\text{C}_2\text{H}_4$ . Hierarchically macroporous–mesoporous (HMMP) Cu/Zn alloy catalysts, prepared through interfacial self-assembly, facilitated the

selective synthesis of liquid C<sub>2</sub> products [111]. The optimized HMMP Cu<sub>5</sub>Zn<sub>8</sub> showed a high C<sub>2</sub>H<sub>5</sub>OH selectivity of 46.6%, an acetate selectivity of 11.7%, and a current density of 3.6 mA·cm<sup>-2</sup> at -0.8 V<sub>RHE</sub>. Based on experiments and DFT calculations, the researchers found that electron-rich Cu in HMMP Cu/Zn catalysts promoted the adsorption of CO<sub>2</sub> while inhibiting the adsorption of H<sub>2</sub>. The amount of Zn in the Cu/Zn alloy controlled the C–C coupling trend. Additionally, the interface of the Cu–Zn catalyst affects the distribution of C<sub>2</sub> in the CO<sub>2</sub>RR [112]. Koper et al. [113] systematically studied the effect of the roughness factor (RF), chemical composition, and morphology of a Cu<sub>x</sub>Zn<sub>y</sub> alloy on the distribution of C<sub>2+</sub> products from CO<sub>2</sub>RRs. They demonstrated that the C–C coupling in the CO<sub>2</sub>RR process depends mainly on the shape of Cu<sub>x</sub>Zn<sub>y</sub> alloy. More specifically, nanocubes of Cu and Cu<sub>x</sub>Zn<sub>y</sub> exhibited the highest Faraday efficiency for C<sub>2+</sub> products, wherein they far outperformed the catalyst with a flat surface, nanospheres, nanodendrites, and nanocauliflowers (Figure 8b–d). In addition, the Faraday efficiency for the C<sub>2+</sub> products increased with the increased in the roughness factor and the content of Zn (Figure 8e). Cuenya et al. [135] used in situ extended X-ray absorption fine structure (EXAFS) and demonstrated that the distribution of products from the CO<sub>2</sub>RR was determined by the composition and structure of the Cu–Zn catalyst. They found that the shorter interatomic distances of Cu–Zn nanoparticles benefited the formation of CH<sub>4</sub>, while the longer Cu–Zn distances favored the generation of CO, which was further reduced to C<sub>2+</sub>.

### 3.2.2. Zn–Ag Bimetallic Materials

Both Ag and Zn are relatively selective for CO<sub>2</sub>RRs to CO. Ag, as a noble metal, shows better catalytic activity and selectivity for CO than the non-precious Zn metal, and it has a lower overpotential [136]. By taking advantage of the synergistic effect between different metals, Ag–Zn alloys could exhibit better catalytic properties for CO<sub>2</sub>RRs with lower costs [137]. For example, Jaramillo et al. reported the electroreduction of CO<sub>2</sub>, which was catalyzed by polycrystalline Ag–Zn foil in a 0.1 M KHCO<sub>3</sub> solution [115]. They found that CH<sub>3</sub>OH and CH<sub>4</sub> were formed at approximately -1.43 V<sub>RHE</sub>, along with a low Faraday efficiency. They suggested that, due to the clearly different oxygen binding energies on Ag and Zn, Ag acts as a binding site for carbon atoms during the reduction of CO<sub>2</sub>, whereas Zn acts as an oxyphilic site, thereby allowing the selective stabilization of surface intermediates at the oxygen termini, which ultimately leads to the enhancement of >2e<sup>-</sup> products through CO<sub>2</sub> reduction [115]. In terms of the main product CO, the Ag–Zn alloy did not exhibit good performance compared to pure Zn and Ag. The researchers designed a Zn<sub>0.87</sub>Ag<sub>0.13</sub> alloy catalyst with a 3D hierarchical layered structure and investigated the effect of its composition (pure Zn, Zn<sub>0.87</sub>Ag<sub>0.13</sub>, and Ag), and thickness (100 nm and 75 μm) on the propensity to generate CO [114]. They found that, although the Zn<sub>0.87</sub>Ag<sub>0.13</sub> alloy contained less silver, it could retain the same activity as pure Ag. The 75 μm Zn<sub>0.87</sub>Ag<sub>0.13</sub> GDE exhibited the highest CO Faraday efficiency of 96% at 100 mA·cm<sup>-2</sup> and maintained a FE<sub>CO</sub> above 85% at a set current density of 500 mA·cm<sup>-2</sup>. By constructing a multiphysics model, they suggested that a thick catalyst layer (75 μm) effectively encloses the incoming CO<sub>2</sub>, due to which more CO<sub>2</sub> is converted to CO by reductive reactions compared to parasitic CO<sub>2</sub> consumption, which leads to a higher catalyst activity. On the other hand, a thinner catalyst layer (100 nm) loses a significant amount of CO<sub>2</sub> into the electrolyte and yields a lower rate of reduction of CO<sub>2</sub>. In other words, the performance of the CO<sub>2</sub>RR of different thicknesses of Zn<sub>0.87</sub>Ag<sub>0.13</sub> catalysts depends mainly on the local amounts of CO<sub>2</sub> around the active sites. Recently, it was demonstrated that high curvature nanoneedle structures enhanced the catalytic performance of CO<sub>2</sub>RRs through their field-induced CO<sub>2</sub> concentration [138,139]. Porous Zn conformal coatings on dendritic Ag nanoneedles (AgNNs@Zn) that were synthesized by vacuum thermal evaporation [116] exhibited a CO Faraday efficiency of 91% at -0.86 V<sub>RHE</sub>. DFT calculations showed that the constructed Ag–Zn interface significantly stabilized the key intermediate species of \*COOH for generating CO from the CO<sub>2</sub>RR, thus resulting in a high selectivity of the CO product.

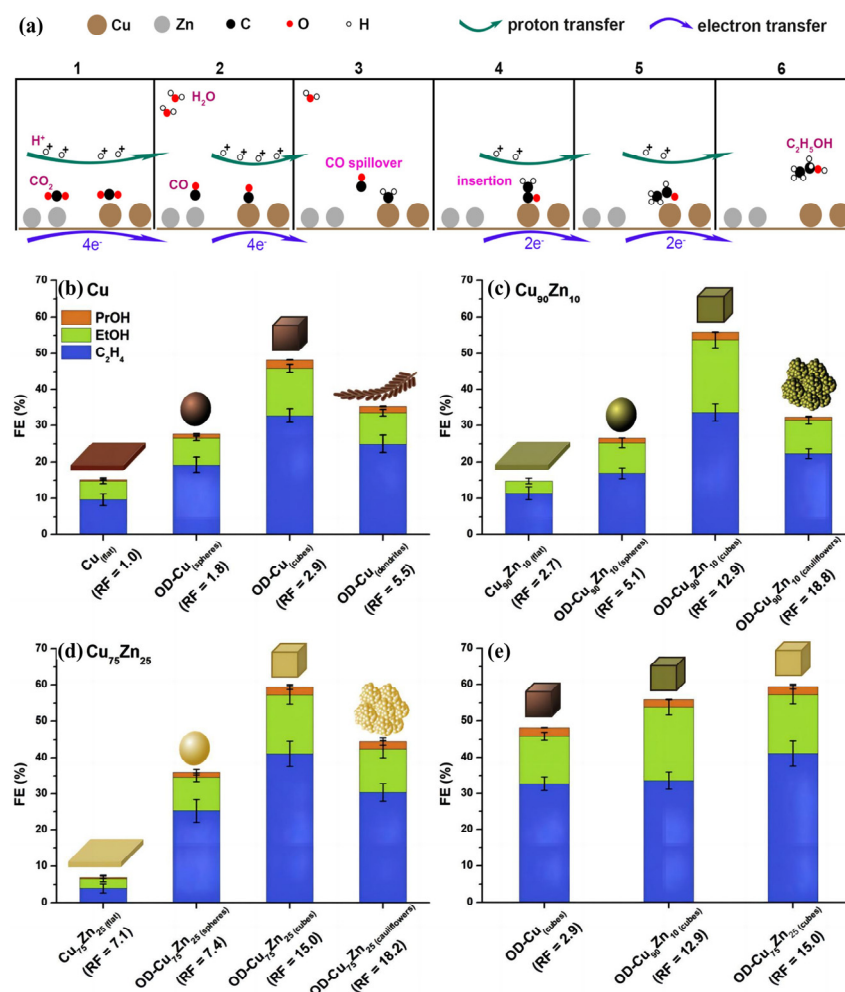


**Figure 8.** (a) Proposed mechanism for the electroreduction of CO<sub>2</sub> to ethanol on Cu<sub>x</sub>Zn catalysts: stage 1 → 2, reduce CO<sub>2</sub> to CO on Cu and Zn, respectively ( $2\text{CO}_2 + 4\text{H}^+ + 4\text{e}^- \rightarrow 2\text{CO} + 2\text{H}_2\text{O}$ ); stage 2 → 3, reduce CO molecule to \*CH<sub>2</sub> on Cu ( $\text{CO} + 4\text{H}^+ + 4\text{e}^- \rightarrow * \text{CH}_2 + \text{H}_2\text{O}$ ); stage 3 → 4, CO insert into the bond between the Cu surface and \*CH<sub>2</sub>, to form \*COCH<sub>2</sub> ( $\text{CO} + * \text{CH}_2 \rightarrow * \text{COCH}_2$ ); stage 4 → 5, reduce \*COCH<sub>2</sub> to CH<sub>3</sub>CHO ( $* \text{COCH}_2 + 2\text{H}^+ + 2\text{e}^- \rightarrow \text{CH}_3\text{CHO}$ ); stage 5 → 6, reduce CH<sub>3</sub>CHO to CH<sub>3</sub>CH<sub>2</sub>OH ( $\text{CH}_3\text{CHO} + 2\text{H}^+ + 2\text{e}^- \rightarrow \text{CH}_3\text{CH}_2\text{OH}$ ). Reprinted with permission from Ref. [124]. Copyright © 2023, American Chemical Society. (b) FE on Cu(flat), OD-Cu(spheres), OD-Cu(cubes), and OD-Cu(dendrites), (c) FE on Cu<sub>90</sub>Zn<sub>10</sub> (flat), OD-Cu<sub>90</sub>Zn<sub>10</sub>(spheres), OD-Cu<sub>90</sub>Zn<sub>10</sub>(cubes), and OD-Cu<sub>90</sub>Zn<sub>10</sub>(cauliflowers), (d) FE on Cu<sub>75</sub>Zn<sub>25</sub>(flat), OD-Cu<sub>75</sub>Zn<sub>25</sub>(spheres), OD-Cu<sub>75</sub>Zn<sub>25</sub>(cubes), and OD-Cu<sub>75</sub>Zn<sub>25</sub>(cauliflowers), and (e) OD-Cu(cubes), OD-Cu<sub>90</sub>Zn<sub>10</sub> (cubes), and OD-Cu<sub>75</sub>Zn<sub>25</sub>(cubes) at −1.1 V vs. RHE [113].

### 3.2.3. Zn–Pd and Zn–Pt

Palladium (Pd) is a unique element that can convert CO<sub>2</sub> to HCOO<sup>-</sup> and CO in the low and high reduction potential regions, respectively, and, therefore, palladium electrocatalysts have attracted a lot of attention [26,140]. In order to achieve a high FE for producing HCOOH, Gunji et al. [101] synthesized atomically disordered Pd–Zn bimetallic alloys and investigated the electrocatalytic selectivity for the reduction reaction of CO<sub>2</sub>. An FE of 99.4% for the production of HCOO<sup>-</sup> at −0.1 V<sub>RHE</sub> on PdZn NPs was obtained. Compared to pure Pd, the selectivity for formate on the Pd–Zn catalysts was enhanced due to the lower *d*-band center of the Pd in the Pd–Zn alloy.

A feasible strategy for enhancing the selective reduction of CO<sub>2</sub> is to employ metal-alloy-based g-C<sub>3</sub>N<sub>4</sub> composites in the CO<sub>2</sub>RR, thus exploiting the enhanced electrical conductivity and strong synergistic effects between the alloy metals [102,141]. Hung

et al. [102] prepared Pd–Zn/g-C<sub>3</sub>N<sub>4</sub> nanocomposites (Pd–Zn–GCN) using a simple hydrothermal reduction reaction, and their activity towards electrocatalytic CO<sub>2</sub> reduction was investigated. With a metal loading of 4% of the composite Pd–Zn–GCN, the highest catalytic activity for the conversion of CO<sub>2</sub> to CO was achieved with an average FE of 93.6%, as well as a CO partial current density of 4.4 mA·cm<sup>−2</sup> at a thermodynamic overpotential of −0.79 V<sub>RHE</sub>. In addition, Pd–Zn–GCN showed good stability. The excellent catalytic activity of the Pd–Zn–GCN is attributed to its relatively large electrochemically activated surface area, *d*-band center transfer, optimal work function, and strain engineering [101,142] achieved through the cooperative action of the Pd–Zn and g-C<sub>3</sub>N<sub>4</sub> [102].

Recently, Roy's group developed Pt–Zn nanoalloys for CO<sub>2</sub>RRs [104]. They synthesized the active sites of intermetallic Pt–Zn nanoalloys (Pt–Zn/C, Pt<sub>3</sub>Zn/C, and Pt<sub>*x*</sub>Zn/C (1 < *x* < 3)) using the thermal decomposition of metal organic backbone (MOF) precursors. According to their experiments, the onset reduction potentials of HER for PtZn/C, Pt<sub>*x*</sub>Zn/C, and Pt<sub>3</sub>Zn/C were −1.02, −1.10, and −0.85 V, respectively. As for the CO<sub>2</sub>RR, the onset of reduction was observed at −0.96, −0.68, and −0.70 V, respectively. The reduction onset potential of CO<sub>2</sub> was more positive in Pt<sub>*x*</sub>Zn/C. In addition, the separation of the onset reduction potential between HER and the CO<sub>2</sub>RR was the maximum (0.42 V), thereby indicating a better catalytic activity of Pt<sub>*x*</sub>Zn/C. The highest FE for CH<sub>3</sub>OH of 81.4% was achieved at −0.9 V<sub>RHE</sub> over the Pt<sub>*x*</sub>Zn/C catalyst. In order to reveal the efficient CO<sub>2</sub>RR reaction mechanism and kinetics of the structure-sensitive Pt<sub>*x*</sub>Zn/C, a possible pathway for the reduction of CO<sub>2</sub> on Pt<sub>*x*</sub>Zn/C nanoalloys was proposed (Figure 9). The main branching point that determined the selectivity of the product for CH<sub>3</sub>OH or CH<sub>3</sub>COOH was controlled by the relative strength of the surface \*−OCH<sub>3</sub> bond relative to the \*O−CH<sub>3</sub> bond [143]. Pt<sub>*x*</sub>Zn promotes the transfer of single electrons to the adsorbed CO<sub>2</sub> and better binds the intermediate CO<sub>2</sub><sup>•−</sup> to its surface. Moreover, the weaker interaction between O and the surface resulted in a higher CH<sub>3</sub>OH selectivity of Pt<sub>*x*</sub>Zn.

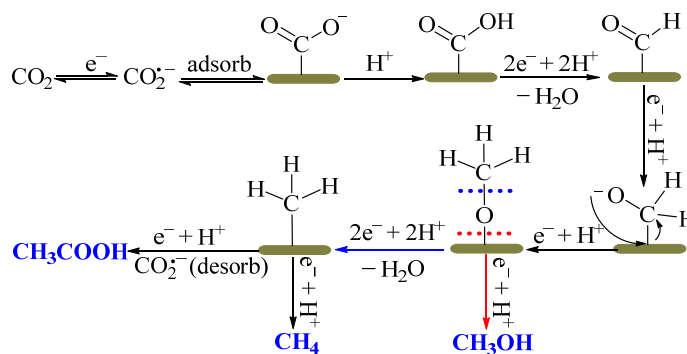


**Figure 9.** Probable mechanism of CO<sub>2</sub>RR with product distribution over intermetallic nanoalloys [104].

### 3.2.4. Other Zn-Based Bimetallic Materials

The reaction intermediate of \*COOH or \*OCOH in the CO<sub>2</sub>RR pathway to CO or formic acid is known to be regulated on Zn, which is due to its moderate carbophilic or oxygenophilic nature when attached to other guests. In addition, Zn has a weak \*H binding capacity. Therefore, Zn is targeted as an important player in the regulation of product selectivity. By mixing metals at the atomic level, catalysts with excellent selectivity for CO or formic acid are designed. For instance, bimetallic indium–zinc (In–Zn) nanocrystals were synthesized using the in-situ reduction of In<sub>2</sub>O<sub>3</sub>–ZnO nanocomposites during CO<sub>2</sub>RRs with tunable interfacial exposure. It was observed that the interfacial position of Zn<sub>0.95</sub>In<sub>0.05</sub> favored the production of HCOOH, as the indium islands on the Zn(002) facet made it easier to release the adsorbed \*OCHO intermediates [99]. The highest FE for HCOOH of 95% was achieved at −1.2 V<sub>RHE</sub> with the Zn<sub>0.95</sub>In<sub>0.05</sub> catalyst. This work suggested that the productivity and selectivity of HCOOH could be improved by controlling the composition

of the In–Zn. The Zn–Bi bimetallic catalyst, obtained by modifying the bismuth element on the Zn catalyst, demonstrated both the selectivity and the overpotential for the formation of HCOOH through the reduction of CO<sub>2</sub> over the Zn–Bi catalyst. The performance of the catalyst could be varied by changing the composition ratio of the Bi [98]. The formate's Faraday efficiency reached up to 94% at  $-0.8 V_{\text{RHE}}$ , which was comparable to the results of the In–Zn catalyst [99]. Since metal–metal bifunctional interfaces and grain boundaries (GBs) comprise more low-coordinated active sites, the bifurcated \*OCHO intermediates are more stable at these sites than on single-crystal metal surfaces, thus allowing higher catalytic activity for the electroreduction of CO<sub>2</sub> to formate. The excellent performance of the Zn–Bi bimetallic catalyst was attributed to a high density of active sites offered by the metal–metal bifunctional interfaces and grain boundaries [98].

Tin (Sn) is a typical catalyst for the selective generation of formate from CO<sub>2</sub>RRs due to its moderate binding energy to \*OCHO [144–146]. The introduction of Sn to Zn-based catalysts can alter their inherent electrochemical properties to reduce CO<sub>2</sub> to CO and achieve higher yields of formate. The transfer of electrons from Zn to Sn reduces the *d*-band center of Sn and improves the surface adsorption properties and formic acid selectivity of the \*OCHO intermediate, thus resulting in more reliable surface adsorption of \*OCHO intermediates and high formate selectivity [100]. Huo et al. reported a Zn–Sn catalyst that was supported on bulk Zn foil and exhibited an enhanced HCOOH selectivity of 94% in 0.5 M KHCO<sub>3</sub> at  $-1.06 V_{\text{RHE}}$  [100]. Subsequently, bimetallic Zn<sub>3</sub>Sn<sub>2</sub> catalysts prepared by in situ electrochemical reduction of heterostructured Zn<sub>x</sub>Sn<sub>y</sub>O<sub>z</sub> nanoparticles loaded on CNTs [106] achieved a 96.7% FE for formate at  $-1.1 V_{\text{RHE}}$ . DFT calculations showed that the adsorption of \*OCHO could be stabilized due to the low limiting free energy of the Zn (101)/Sn (200) hybrid surface (0.52 eV), which promoted its high selectivity to formate. Bimetallic Zn–Sb nanoparticles, supported on carbon nanotubes, were also reported by their group, and produced formates at 92% to the utmost extent at  $-1.0 V_{\text{RHE}}$  [104].

### 3.3. Oxide-Derived Zn Catalysts

ZnO can stabilize carboxylate intermediates and is considered a promising catalyst for CO<sub>2</sub>RRs [147]. However, ZnO catalyst suffers from poor selectivity and sluggish reaction kinetics [148,149]. In order to enhance the catalyst performance of ZnO catalysts, considerable efforts have been devoted to structural regulation [150], oxygen vacancy [149], atoms doping [151], and alloying with other metals [122].

Wu et al. [152] reported a heterogeneous structure of ZnO nanosheets/Zn prepared using a hydrothermal method, in which a large number of (1100) edge surfaces were exposed. They suggested that the exposed (1100) edge facets promoted the catalytic performance of ZnO by accelerating the transfer of electrons and increasing the number of active sites. Gao et al. [153] reported that the CO<sub>2</sub>RR performance of ZnO nanosheets constructed by the solvothermal method could be improved by varying the molar ratio of alkali sources (urea, sodium hydroxide, and ammonia) to zinc nitrate hexahydrate. The optimized ZnO-UR showed good catalyst performance with a CO Faraday efficiency of 88% and a current density of 10 mA·cm<sup>-2</sup> at  $-0.95 V_{\text{RHE}}$  in 0.5 M aqueous KHCO<sub>3</sub>. These works indicated that structural regulation offered a robust approach to enhance the CO<sub>2</sub>RR performance of ZnO catalysts.

Recently, another effective strategy to promote the activation of CO<sub>2</sub> by introducing oxygen vacancies into electrocatalysts with electron-rich surfaces has been demonstrated [154,155]. For example, the CO<sub>2</sub>RR performance of ZnO was enhanced by the introduction of oxygen vacancies in nanosheets of ZnO [155]. The authors showed that ZnO nanosheets, which are rich in oxygen vacancies (*V*<sub>O</sub>-rich ZnO), exhibited a CO Faraday efficiency of 83% and a current density of 16.1 mA·cm<sup>-2</sup> at  $-1.1 V_{\text{RHE}}$  in 0.1 M KHCO<sub>3</sub>, which exceeded the performance of *V*<sub>O</sub>-poor (73%, 12 mA·cm<sup>-2</sup>) and pristine ZnO (44%, 7 mA·cm<sup>-2</sup>) under the same conditions. The excellent performance of *V*<sub>O</sub>-rich ZnO nanosheets was mainly attributed to the introduction of oxygen vacancies, which enhanced the binding of CO<sub>2</sub> and reduced the Gibbs free energy of \*COOH [155,156]. In

addition, the introduction of other components can also improve the performance of the CO<sub>2</sub>RR of oxide-derived Zn catalysts. For example, CuO doped on ZnO hollow microspheres enhanced the CO Faraday efficiency. The highest value of 90.7% was achieved for 3CuO/ZnO at  $-1.2 V_{RHE}$ , which was approximately twice as high as for ZnO [157]. Zeng et al. [157] suggested that the introduction of a small amount of copper would distort the ZnO crystal conformation through the interaction of elements, thereby weakening the Zn–O bond, favoring the formation of surface defects, and promoting the CO<sub>2</sub> activation during the initial reduction reaction. Li et al. [125] reported that CO spillover effects were enhanced by the uniform distribution of Cu and Zn atoms in the electrocatalysts. The reduced ZnO nanoparticles provide additional CO to the reduced CuO nanoparticles, thereby increasing the \*CO surface coverage for C–C coupling and the selective production of C<sub>2</sub>H<sub>4</sub> and C<sub>2</sub>H<sub>5</sub>OH.

Kang et al. [158] comprehensively investigated the effect of nanomorphology and silver doping on the CO<sub>2</sub>RR performance of ZnO. Different morphologies such as nanospheres, nanorods, and nanosheets (Figure 10a–c) of ZnO were prepared using the hydrothermal method. Among them, the ZnO nanorod showed the best performance with a Faraday efficiency of 68.3% (Figure 10d) for CO and a current density of  $100 \text{ mA}\cdot\text{cm}^{-2}$  at  $-0.76 V_{RHE}$ . The excellent properties of ZnO nanorods were ascribed to higher O-deficient surface conditions in the higher surface area, which activated the adsorption of \*CO [149,159]. Surface field emission scanning electron microscopy (FE-SEM) images of ZnO nanorods doped with different concentrations (1, 3, and 5 atom%) of AgNO<sub>3</sub> are shown in Figure 10e–g. The overall ZnO morphology remained unchanged after Ag doping before the CO<sub>2</sub>RR testing. The highest FE<sub>CO</sub> value of 91.9% was obtained for 1 atom% Ag-doped ZnO nanorods at  $150 \text{ mA}\cdot\text{cm}^{-2}$  and  $-0.76 V_{RHE}$  (Figure 10h), thus indicating an improvement in CO selectivity of about 23%, even at high current densities. Meanwhile, Ag-doped ZnO could maintain a stable performance for up to 10 h, which is a great improvement compared to the performance of ZnO for 4 h. Ag doping could achieve \*CO adsorption through the localized electronic structure of ZnO nanorods. In addition, Ag sites can provide good mass transfer due to a low interfacial charge transfer resistance ( $R_{CT}$ ). The study demonstrates that the morphological characteristics of the electrocatalyst are key controlling factors in the CO<sub>2</sub>RR and can be further improved by appropriate metal doping.

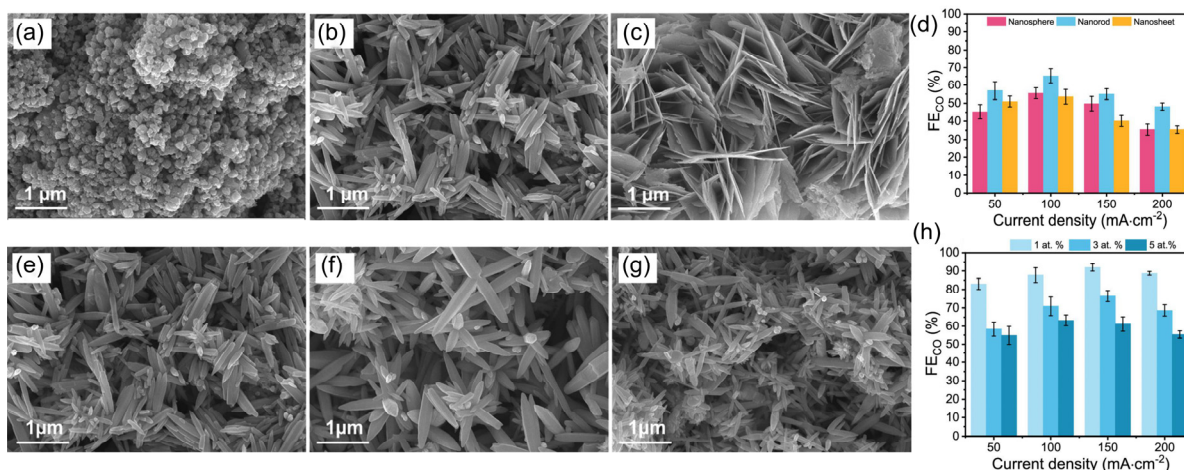


**Figure 10.** (a) FE-SEM of nanosphere ZnO, (b) FE-SEM of nanorod ZnO, (c) FE-SEM of nanosheet ZnO electrocatalysts before CO<sub>2</sub>RR, respectively. (d) FEs (%) of CO at different current densities on ZnO electrocatalysts with different morphologies. (e) 1 atom%, (f) 3 atom%, and (g) 5 atom% of Ag doping and (h) FEs (%) of CO at different current densities on ZnO electrocatalysts with different Ag doping [158]. Reproduced with permission from Ref. [158]. Copyright © 2023, American Chemical Society.

### 3.4. Single/Dual Zn Atom Catalysts

#### 3.4.1. Single Zn Atom Catalysts

Single-atom catalysts (SACs) [160–164] are atomically dispersed metal- and nitrogen-co-doped carbon materials (M-N-C, M = Fe, Co, Ni, and Cu) that have been extensively studied in CO<sub>2</sub>RRs due to their high atomic efficiency and catalytic activity. For example, the Fe catalyst (Fe<sup>3+</sup>-N-C) [165] derived from an Fe-doped Zn 2-methyl imidazolate framework using pyrolysis exhibited a high selectivity of over 90% for CO with a current density of 94 mA·cm<sup>-2</sup> at -0.45 V<sub>RHE</sub> in the flow-type cell. Moreover, Ni-N/C SAC derived from NiPc-CN [166] showed a higher FE of CO > 96% and stability. Zn-NC has experienced little progress compared with other transition metal monoatoms due to its low melting and boiling points and its fully filled 3d orbital configuration [167]. Several studies have shown that Zn-based single-atom catalysts (SACs) can efficiently catalyze the conversion of CO<sub>2</sub>. For instance, Xu et al. [168] reported that single-atom Zn catalysts (ZnN<sub>4</sub>/C) promoted CO<sub>2</sub>RR to produce CO with a maximum Faraday efficiency of 95% for CO at -0.43 V<sub>RHE</sub> in a 0.5 M aqueous KHCO<sub>3</sub> solution. Meanwhile, ZnN<sub>4</sub>/C exhibited significant durability (>75 h) and a large turnover frequency (9969 h<sup>-1</sup>). DFT calculations suggested that the excellent CO<sub>2</sub>RR performance of ZnN<sub>4</sub>/C may be due to the low energy barrier in the rate-determining step of COOH\* formation at Zn-N<sub>4</sub> sites. The formation of the Zn-N<sub>4</sub> active site was responsible for the superior performance of the Zn single-atom catalyst [169]. Xin et al. reported a microporous N-doped carbon-loaded Zn single-atom catalyst (SA-Zn/MNC) that was prepared using the dissolution carbonation method, and it exhibited a Faraday efficiency of 85% for a CO<sub>2</sub>RR to CH<sub>4</sub> with a partial current density of about 31.8 mA·cm<sup>-2</sup> and a stability of over 35 h at -1.8 V<sub>SCE</sub> [170]. DFT calculations revealed that, during the CO<sub>2</sub>RR process, the O atom (rather than the carbon atom) in \*OCHO preferred to form chemical bonds with Zn SAs, thereby hindering the formation of CO and contributing to the formation of CH<sub>4</sub>. The curvature of a Zn-N<sub>x</sub> site was used by Lin et al. [171] and Lv et al. [172] as a way to enhance the CO<sub>2</sub>RR to CO by increasing the electron density of the Zn's 3d orbital. Recently, Daasbjerg et al. [167] reported nitrogen-anchored low-valent Zn<sup>δ+</sup> monatoms (Zn<sup>δ+</sup>-NC) containing saturated Zn-N<sub>4</sub> and unsaturated Zn-N<sub>3</sub> sites, which were prepared using the pyrolysis of Zn-containing precursors in a nitrogen source. The Zn<sup>δ+</sup>-NC catalyst displayed almost 100% selectivity for CO with a small overpotential of 310 mV. It is noteworthy that a record current density of 1 A·cm<sup>-2</sup> was obtained when the Zn<sup>δ+</sup>-NC catalyst was used in a flow cell electrolyzer. According to the DFT calculations, the formation of COOH\* was more favorable for the unsaturated Zn-N<sub>3</sub> than for the Zn-N<sub>4</sub>. In addition, the key intermediate of COOH\* had a Zn-C bond length of 2.012 Å and 1.974 Å on Zn-N<sub>4</sub> and Zn-N<sub>3</sub> sites, respectively. The shorter Zn-C bond length of Zn-N<sub>3</sub> indicates a stronger interaction and charge transfer between the Zn atom and COOH\*, which resulted in a better stabilization of COOH\* and facilitated the reduction of CO<sub>2</sub> to CO.

Tandem catalysis provides an efficient strategy for the electroreduction of CO<sub>2</sub> to C<sub>2+</sub> products, whereby CO<sub>2</sub> is first reduced at one class of active sites to produce a large amount of CO, which subsequently diffuses to another class of active sites for further reduction to C<sub>2+</sub> products [161]. Wang et al. reported that the CoPc@Zn-N-C tandem catalyst enhanced the reduction of CO<sub>2</sub> to CH<sub>4</sub> with a Faraday efficiency of 18.3% and current density of 44.3 mA·cm<sup>-2</sup> at -1.24 V<sub>RHE</sub> in 1 M aqueous KOH solution [173]. DFT calculations demonstrated that the tandem catalytic process was as follows: CO was first achieved by the reduction of CO<sub>2</sub> on CoPc, which then migrated to Zn-N-C on ZnN<sub>4</sub> and was reduced to CH<sub>4</sub>, with the pathway involving \*CH intermediates. Through the Langmuir-Hinshelwood mechanism, the adsorption of \*H on ZnN<sub>4</sub> as a reservoir is key to enhancing the formation of \*CHO, which is essential for high CH<sub>4</sub> yields [173].

#### 3.4.2. Dual Zn Atom Catalysts

Dual-atomic-site catalysts (DASCs) [174], which harbor the advantages of monatomic catalysts, can also achieve more complex and tunable atomic structures by adjusting another

neighboring metal. As a deeper extension of SACs, DASCs have recently attracted much interest. Diatomic Zn–Co monomers that are loaded onto N-doped carbon (ZnCoNC) and prepared using pyrolysis [175] showed a high Faraday efficiency for CO of 93.2% with a CO partial current density of  $26 \text{ mA}\cdot\text{cm}^{-2}$  at  $-0.5 \text{ V}_{\text{RHE}}$ . The elemental content of ZnCoC was confirmed using inductively coupled plasma photoemission spectroscopy (ICP-AES) and X-ray photoelectron spectroscopy (XPS). Coordination environments and electronic effects of Zn/Co were examined using an XANES (X-ray absorption near-edge structure) and EXAFS (X-ray absorption fine structure measurements). The authors of the study found that both Zn and Co were coordinated on NC in a four-coordinated form (Zn–N<sub>4</sub> and Co–N<sub>4</sub>), and that there was essentially no direct metal–metal bonding or metal–C coordination between the Zn and Co. They concluded that adjacent Zn/Co in the ZnCoNC interacted indirectly and electronically through N atoms. DFT calculations showed that the adjacent Zn/Co electron effect reduced the energy barrier to the generation of \*COOH, thereby making it easier to produce CO.

Du et al. [176] prepared Zn–La DASCs that were loaded with carbon nitride nanosheets (ZnLaCN) using impregnation and annealing for CO<sub>2</sub>RRs. Syngas could be produced within a large range of CO/H<sub>2</sub> ratios (0.14~1) by tuning the ratio of Zn and La atomic sites. In addition, the ZnLa-1/CN electrocatalyst allowed for the preparation of syngas with CO/H<sub>2</sub> ratio of 0.5 within a wide potential range with a total FE of 80% for the CO<sub>2</sub>RR and good stability. The coordination environments of the dual atomic Zn/La were verified to be Zn–N, La–N, and La–C bonding with coordination numbers of 2.6, 6, and 10, respectively. DFT calculations confirmed that the Zn sites were primarily responsible for the activation of CO<sub>2</sub> to CO, while the La site promoted the evolution of H<sub>2</sub>.

Another study reported that BiZn/NCs [177] that were derived from BiZn-MOFs using pyrolysis and carbonization could facilitate the CO<sub>2</sub>RR to syngas with a tunable CO/H<sub>2</sub> ratio (0.20~2.92) in the applied potential range, which is favorable for the synthesis of CH<sub>3</sub>OH and Fischer–Tropsch reactions [176]. They demonstrated that both Bi and Zn were coordinated on NC in a four-coordinated form (Bi–N<sub>4</sub> and Zn–N<sub>4</sub>) with the absence of Bi–Bi and Zn–Zn bonds. Additionally, the coordination environment of Bi and Zn in BiZn/NCs was not affected by the variation in Bi/Zn ratio in MOFs.

#### 4. Conclusions and Future Perspectives

A sustainable carbon cycle is essential to sustain the healthy evolution of life worldwide. However, human activities, especially the increasing demand of energy, have led to an overconsumption of fossil fuels, which severely affect the well-established balance of the natural carbon cycle. Given the threat of excessive CO<sub>2</sub> emissions, negative carbon technologies are now increasingly in demand. In this quest, the CO<sub>2</sub>RRs that are powered by renewable electricity to prepare high-value-added fuels or chemicals have been widely recognized as a promising approach to balance the carbon cycle, thus resulting in sustainable environmental and economic benefits. This is why the research of CO<sub>2</sub>RRs has attracted more and more attention [178].

This review assessed recent progress in the innovation and development of Zn-based electrocatalysts for CO<sub>2</sub>RRs to fuels. Various Zn-based catalysts have been introduced, such as monometallic Zn, Zn-based bimetallic, oxide-derived Zn catalysts, and single/dual Zn atom catalysts. In addition, modifications to Zn-based electrocatalysts, such as engineering crystal facets, tuning morphologies and components, introducing lattice defects and ligands, or constructing single-atom catalysts (SACs), can enhance the activity of CO<sub>2</sub>RRs. Some electrocatalysts have shown excellent catalytic activity and selectivity, as well as suitable levels of stability during the CO<sub>2</sub>RRs (Tables 2 and 3). Although some remarkable advances have been made in the electroreduction of CO<sub>2</sub> using Zn-based catalysts, several challenges in this research area need to be overcome:

- (1) Most Zn-based catalysts for the CO<sub>2</sub>RRs catalyze CO<sub>2</sub>-to-CO conversions. However, more efforts should be devoted to exploring C–C coupling. The adjustment of product selectivity during CO<sub>2</sub>RRs could be achieved using the alloying strategy. Furthermore,

- the surface binding strength could be altered using the alloying strategies through electronic and geometric effects, thereby enhancing the availability of surface-confined carbon species and stabilizing key reduction intermediates [85]. However, it is still extremely difficult to achieve the complete selectivity of one product only through the alloying strategy. Therefore, it can be combined with other catalyst design strategies.
- (2) A thorough understanding of atomistic structure–performance relations over Zn-based catalysts is still missing, which hinders the rational design of more efficient catalysts. In combination with various in situ/operando characterization techniques and theoretical calculations [179], it is expected that the catalyst structure, electronic states, and reaction intermediates in the same reaction process will be investigated, which will provide valuable insight into the conformational relationships and reaction mechanisms of catalysts.
  - (3) The stability of the catalyst is one of the essential elements for commercial applications. Most Zn-based catalysts to date have a lifetime of less than one day, which is well below the lifetime required for commercial applications. Therefore, the degradation mechanism of the catalysts and the corresponding solutions need to be further investigated. Anchoring the zinc-based material on a specific substrate could improve the stability of the catalyst through the interaction of the Zn-based material with the substrate.
  - (4) The practical application of CO<sub>2</sub> electrolysis is greatly hindered by its complex electron transfer, multiple competing pathways, and low rate of diffusion of CO<sub>2</sub> [180]. From a catalyst perspective, it is necessary to rationally design electrocatalysts to overcome the energy barriers of CO<sub>2</sub> activation and intermediation.

In short, although many challenges remain to be overcome for Zn-based catalysts in CO<sub>2</sub>RRs, they are still one of the promising types of catalysts to address the conversion and utilization of CO<sub>2</sub>. As catalysts continue to be designed and developed, the current densities of CO [181–191], C<sub>2</sub>H<sub>4</sub> [182,192,193], and C<sub>2+</sub> [180,194–196] have reached the ampere level (Figure 11). It is believed that the prospect of commercial applications of CO<sub>2</sub>RRs for the production of clean fuels and chemicals will be realized in the near future.

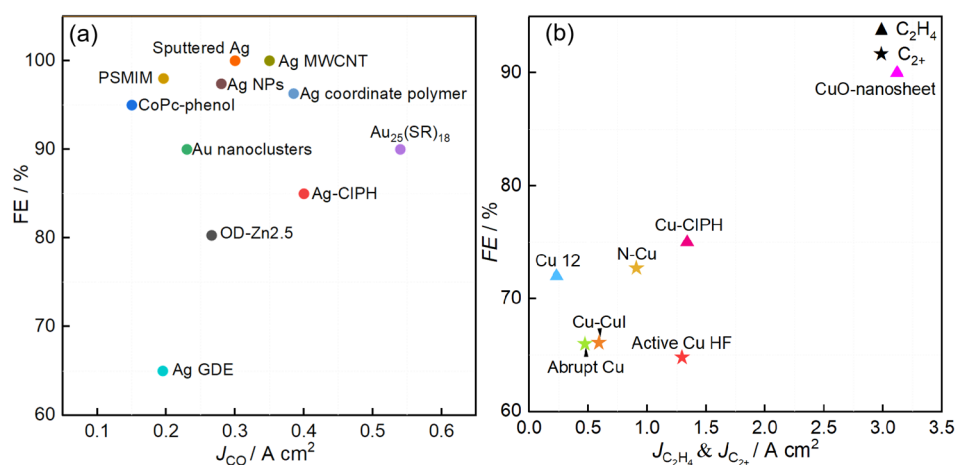


**Figure 11.** Partial current density and Faraday efficiency of (a) CO, (b) C<sub>2</sub>H<sub>4</sub>, and C<sub>2+</sub> products in CO<sub>2</sub>RRs with state-of-the-art catalysts.

**Author Contributions:** Conceptualization, L.W. (Laxia Wu) and J.L.; methodology and software, C.G.; data curation, Y.G. and L.W. (Lin Wu); formal analysis, H.W.; resources and funding acquisition J.L.; writing—original draft preparation, L.W. (Laxia Wu); writing—review and editing, Y.G. and H.W.; visualization and project administration, L.W. (Lin Wu); supervision, J.L. and H.W. All authors have read and agreed to the published version of the manuscript.

**Funding:** This work was financially supported by the National Natural Science Foundation of China (Nos. 21902002, 22072046, 22005004) and the Natural Science Program of Anhui Province University (KJ2020A0512).

**Data Availability Statement:** Data openly available in a public repository.

**Conflicts of Interest:** The authors declare no conflict of interest.

## References

1. Ahmed, Z.; Asghar, M.M.; Malik, M.N.; Nawaz, K. Moving towards a sustainable environment: The dynamic linkage between natural resources, human capital, urbanization, economic growth, and ecological footprint in China. *Resour. Policy* **2020**, *67*, 101677. [CrossRef]
2. Opoku, E.E.O.; Dogah, K.E.; Aluko, O.A. The contribution of human development towards environmental sustainability. *Energy Econ.* **2022**, *106*, 105782. [CrossRef]
3. Yaqoob, H.; Teoh, Y.H.; Goraya, T.S.; Sher, F.; Jamil, M.A.; Rashid, T.; Yar, K.A. Energy evaluation and environmental impact assessment of transportation fuels in Pakistan. *Case Stud. Chem. Environ. Eng.* **2021**, *3*, 100081. [CrossRef]
4. Tong, D.; Zhang, Q.; Zheng, Y.; Caldeira, K.; Shearer, C.; Hong, C.; Qin, Y.; Davis, S.J. Committed emissions from existing energy infrastructure jeopardize 1.5 °C climate target. *Nature* **2019**, *572*, 373–377. [CrossRef] [PubMed]
5. Earth System Research Laboratories. Trends in Atmospheric Carbon Dioxide. Global Monitoring Laboratory. Available online: <https://gml.noaa.gov/ccgg/trends/> (accessed on 18 November 2022).
6. Burkart, M.D.; Hazari, N.; Tway, C.L.; Zeitler, E.L. Opportunities and Challenges for Catalysis in Carbon Dioxide Utilization. *ACS Catal.* **2019**, *9*, 7937–7956. [CrossRef]
7. Wei, K.; Guan, H.; Luo, Q.; He, J.; Sun, S. Recent advances in CO<sub>2</sub> capture and reduction. *Nanoscale* **2022**, *14*, 11869–11891. [CrossRef]
8. De Luna, P.; Hahn, C.; Higgins, D.; Jaffer, S.A.; Jaramillo, T.F.; Sargent, E.H. What would it take for renewably powered electrosynthesis to displace petrochemical processes? *Science* **2019**, *364*, eaav3506. [CrossRef]
9. Qiao, J.; Liu, Y.; Hong, F.; Zhang, J. A review of catalysts for the electroreduction of carbon dioxide to produce low-carbon fuels. *Chem. Soc. Rev.* **2014**, *43*, 631–675. [CrossRef]
10. He, M.; Sun, Y.; Han, B. Green Carbon Science: Efficient Carbon Resource Processing, Utilization, and Recycling towards Carbon Neutrality. *Angew. Chem. Int. Ed.* **2022**, *61*, e202112835.
11. Cai, T.; Sun, H.; Qiao, J.; Zhu, L.; Zhang, F.; Zhang, J.; Tang, Z.; Wei, X.; Yang, J.; Yuan, Q.; et al. Cell-free chemoenzymatic starch synthesis from carbon dioxide. *Science* **2021**, *373*, 1523–1527. [CrossRef] [PubMed]
12. Zheng, T.; Zhang, M.; Wu, L.; Guo, S.; Liu, X.; Zhao, J.; Xue, W.; Li, J.; Liu, C.; Li, X.; et al. Upcycling CO<sub>2</sub> into energy-rich long-chain compounds via electrochemical and metabolic engineering. *Nat. Catal.* **2022**, *5*, 388–396. [CrossRef]
13. Jia, S.; Ma, X.; Sun, X.; Han, B. Electrochemical Transformation of CO<sub>2</sub> to Value-Added Chemicals and Fuels. *CCS Chem.* **2022**, *4*, 3213–3229. [CrossRef]
14. Han, N.; Ding, P.; He, L.; Li, Y.; Li, Y. Promises of Main Group Metal-Based Nanostructured Materials for Electrochemical CO<sub>2</sub> Reduction to Formate. *Adv. Energy Mater.* **2019**, *10*, 1902338–1902357. [CrossRef]
15. Sher, F.; Al-Shara, N.K.; Iqbal, S.Z.; Jahan, Z.; Chen, G.Z. Enhancing hydrogen production from steam electrolysis in molten hydroxides via selection of non-precious metal electrodes. *Int. J. Hydrog. Energy* **2020**, *45*, 28260–28271. [CrossRef]
16. Zhang, Y.-J.; Sethuraman, V.; Michalsky, R.; Peterson, A.A. Competition between CO<sub>2</sub> Reduction and H<sub>2</sub> Evolution on Transition-Metal Electrocatalysts. *ACS Catal.* **2014**, *4*, 3742–3748. [CrossRef]
17. Hori, Y.; Kikuchi, K.; Suzuki, S. Production of CO and CH<sub>4</sub> in electrochemical reduction of CO<sub>2</sub> at metal electrodes in aqueous hydrogencarbonate solution. *Chem. Lett.* **1985**, *14*, 1695–1698. [CrossRef]
18. Liu, X.; Li, B.-Q.; Ni, B.; Wang, L.; Peng, H.-J. A perspective on the electrocatalytic conversion of carbon dioxide to methanol with metallomacrocyclic catalysts. *J. Energy Chem.* **2022**, *64*, 263–275. [CrossRef]
19. Zhu, W.; Michalsky, R.; Metin, O.; Lv, H.; Guo, S.; Wright, C.J.; Sun, X.; Peterson, A.A.; Sun, S. Monodisperse Au nanoparticles for selective electrocatalytic reduction of CO<sub>2</sub> to CO. *J. Am. Chem. Soc.* **2013**, *135*, 16833–16836. [CrossRef] [PubMed]
20. Zhu, W.; Zhang, Y.J.; Zhang, H.; Lv, H.; Li, Q.; Michalsky, R.; Peterson, A.A.; Sun, S. Active and selective conversion of CO<sub>2</sub> to CO on ultrathin Au nanowires. *J. Am. Chem. Soc.* **2014**, *136*, 16132–16135. [CrossRef] [PubMed]
21. Chen, Y.; Li, C.W.; Kanan, M.W. Aqueous CO<sub>2</sub> reduction at very low overpotential on oxide-derived Au nanoparticles. *J. Am. Chem. Soc.* **2012**, *134*, 19969–19972. [CrossRef]
22. Liu, S.; Tao, H.; Zeng, L.; Liu, Q.; Xu, Z.; Liu, Q.; Luo, J.L. Shape-Dependent Electrocatalytic Reduction of CO<sub>2</sub> to CO on Triangular Silver Nanoplates. *J. Am. Chem. Soc.* **2017**, *139*, 2160–2163. [CrossRef]
23. Lu, Q.; Rosen, J.; Zhou, Y.; Hutchings, G.S.; Kimmel, Y.C.; Chen, J.G.; Jiao, F. A selective and efficient electrocatalyst for carbon dioxide reduction. *Nat. Commun.* **2014**, *5*, 3242. [CrossRef]
24. Liu, S.; Wang, X.-Z.; Tao, H.; Li, T.; Liu, Q.; Xu, Z.; Fu, X.-Z.; Luo, J.-L. Ultrathin 5-fold twinned sub-25 nm silver nanowires enable highly selective electroreduction of CO<sub>2</sub> to CO. *Nano Energy* **2018**, *45*, 456–462. [CrossRef]
25. Gao, D.; Zhou, H.; Wang, J.; Miao, S.; Yang, F.; Wang, G.; Wang, J.; Bao, X. Size-dependent electrocatalytic reduction of CO<sub>2</sub> over Pd nanoparticles. *J. Am. Chem. Soc.* **2015**, *137*, 4288–4291. [CrossRef]

26. Gao, D.; Zhou, H.; Cai, F.; Wang, J.; Wang, G.; Bao, X. Pd-Containing Nanostructures for Electrochemical CO<sub>2</sub> Reduction Reaction. *ACS Catal.* **2018**, *8*, 1510–1519. [[CrossRef](#)]
27. She, X.; Wang, Y.; Xu, H.; Chi Edman Tsang, S.; Ping Lau, S. Challenges and Opportunities in Electrocatalytic CO<sub>2</sub> Reduction to Chemicals and Fuels. *Angew. Chem. Int. Ed.* **2022**, *61*, e202211396. [[CrossRef](#)] [[PubMed](#)]
28. Ma, W.; He, X.; Wang, W.; Xie, S.; Zhang, Q.; Wang, Y. Electrocatalytic reduction of CO<sub>2</sub> and CO to multi-carbon compounds over Cu-based catalysts. *Chem. Soc. Rev.* **2021**, *50*, 12897–12914. [[CrossRef](#)]
29. Yang, H.; Wang, X.; Hu, Q.; Chai, X.; Ren, X.; Zhang, Q.; Liu, J.; He, C. Recent Progress in Self-Supported Catalysts for CO<sub>2</sub> Electrochemical Reduction. *Small Methods* **2020**, *4*, 1900826. [[CrossRef](#)]
30. Jin, S.; Hao, Z.; Zhang, K.; Yan, Z.; Chen, J. Advances and Challenges for the Electrochemical Reduction of CO<sub>2</sub> to CO: From Fundamentals to Industrialization. *Angew. Chem. Int. Ed.* **2021**, *60*, 20627–20648. [[CrossRef](#)] [[PubMed](#)]
31. Wang, Y.; Huang, N.-Y.; Wang, H.-Y.; Zhang, X.-W.; Huang, J.-R.; Liao, P.-Q.; Chen, X.-M.; Zhang, J.-P. Local Weak Hydrogen Bonds Significantly Enhance CO<sub>2</sub> Electroreduction Performances of a Metal-Organic Framework. *CCS Chem.* **2023**, *5*, 145–151. [[CrossRef](#)]
32. Zheng, Y.; Wang, Y.; Yuan, Y.; Huang, H. Metal-based Heterogeneous Electrocatalysts for Electrochemical Reduction of Carbon Dioxide to Methane: Progress and Challenges. *ChemNanoMat* **2021**, *7*, 502–514. [[CrossRef](#)]
33. Wang, S.; Kou, T.; Baker, S.E.; Duoss, E.B.; Li, Y. Electrochemical Reduction of CO<sub>2</sub> to Alcohols: Current Understanding, Progress, and Challenges. *Adv. Energy Sustain. Res.* **2021**, *3*, 2100131. [[CrossRef](#)]
34. Gao, D.; Arán-Ais, R.M.; Jeon, H.S.; Roldan Cuenya, B. Rational catalyst and electrolyte design for CO<sub>2</sub> electroreduction towards multicarbon products. *Nat. Catal.* **2019**, *2*, 198–210. [[CrossRef](#)]
35. Zhang, B.; Cao, S.; Wu, Y.; Zhai, P.; Li, Z.; Zhang, Y.; Fan, Z.; Wang, C.; Zhang, X.; Hou, J.; et al. Metal-Organic-Framework-Derived Bismuth Nanosheets for Electrochemical and Solar-Driven Electrochemical CO<sub>2</sub> Reduction to Formate. *ChemElectroChem* **2021**, *8*, 880–886. [[CrossRef](#)]
36. Akter, T.; Pan, H.; Barile, C.J. Tandem Electrocatalytic CO<sub>2</sub> Reduction inside a Membrane with Enhanced Selectivity for Ethylene. *J. Phys. Chem. C* **2022**, *126*, 10045–10052. [[CrossRef](#)]
37. Kim, J.; Choi, W.; Park, J.W.; Kim, C.; Kim, M.; Song, H. Branched Copper Oxide Nanoparticles Induce Highly Selective Ethylene Production by Electrochemical Carbon Dioxide Reduction. *J. Am. Chem. Soc.* **2019**, *141*, 6986–6994. [[CrossRef](#)]
38. Baek, Y.; Song, H.; Hong, D.; Wang, S.; Lee, S.; Joo, Y.-C.; Lee, G.-D.; Oh, J. Electrochemical carbon dioxide reduction on copper–zinc alloys: Ethanol and ethylene selectivity analysis. *J. Mater. Chem. A* **2022**, *10*, 9393–9401. [[CrossRef](#)]
39. Chanda, D.; Tufa, R.A.; Aili, D.; Basu, S. Electroreduction of CO<sub>2</sub> to ethanol by electrochemically deposited Cu-lignin complexes on Ni foam electrodes. *Nanotechnology* **2021**, *33*, 055403. [[CrossRef](#)] [[PubMed](#)]
40. Du, J.; Zhang, P.; Liu, H. Electrochemical Reduction of Carbon Dioxide to Ethanol: An Approach to Transforming Greenhouse Gas to Fuel Source. *Chem. Asian J.* **2021**, *16*, 588–603. [[CrossRef](#)]
41. Wu, J.X.; Hou, S.Z.; Zhang, X.D.; Xu, M.; Yang, H.F.; Cao, P.S.; Gu, Z.Y. Cathodized copper porphyrin metal-organic framework nanosheets for selective formate and acetate production from CO<sub>2</sub> electroreduction. *Chem. Sci.* **2019**, *10*, 2199–2205. [[CrossRef](#)]
42. Yu, J.; Wang, J.; Ma, Y.; Zhou, J.; Wang, Y.; Lu, P.; Yin, J.; Ye, R.; Zhu, Z.; Fan, Z. Recent Progresses in Electrochemical Carbon Dioxide Reduction on Copper-Based Catalysts toward Multicarbon Products. *Adv. Funct. Mater.* **2021**, *31*, 2102151. [[CrossRef](#)]
43. Fan, L.; Xia, C.; Yang, F.; Wang, J.; Wang, H.; Lu, Y. Strategies in catalysts and electrolyzer design for electrochemical CO<sub>2</sub> reduction toward C<sub>2+</sub> products. *Sci. Adv.* **2020**, *6*, eaay3111. [[CrossRef](#)]
44. Hou, Y.; Jiang, C.J.; Wang, Y.; Zhu, J.W.; Lu, J.X.; Wang, H. Nitrogen-doped mesoporous carbon supported CuSb for electroreduction of CO<sub>2</sub>. *RSC Adv.* **2022**, *12*, 12997–13002. [[CrossRef](#)] [[PubMed](#)]
45. Wang, G.; Chen, J.; Ding, Y.; Cai, P.; Yi, L.; Li, Y.; Tu, C.; Hou, Y.; Wen, Z.; Dai, L. Electrocatalysis for CO<sub>2</sub> conversion: From fundamentals to value-added products. *Chem. Soc. Rev.* **2021**, *50*, 4993–5061. [[CrossRef](#)] [[PubMed](#)]
46. Li, N.; Wang, X.; Lu, X.; Zhang, P.; Ong, W.J. Comprehensive Mechanism of CO<sub>2</sub> Electroreduction on Non-Noble Metal Single-Atom Catalysts of Mo<sub>2</sub>CS<sub>2</sub>-MXene. *Chemistry* **2021**, *27*, 17900–17909. [[CrossRef](#)]
47. Wang, X.; Hu, Q.; Li, G.; Yang, H.; He, C. Recent Advances and Perspectives of Electrochemical CO<sub>2</sub> Reduction Toward C<sub>2+</sub> Products on Cu-Based Catalysts. *Electrochem. Energy Rev.* **2022**, *5* (Suppl. S2), 28. [[CrossRef](#)]
48. Hori, Y. Electrochemical CO<sub>2</sub> Reduction on Metal Electrodes. *Mod. Asp. Electrochem.* **2008**, *42*, 89–189.
49. Rosen, J.; Hutchings, G.S.; Lu, Q.; Forest, R.V.; Moore, A.; Jiao, F. Electrodeposited Zn Dendrites with Enhanced CO Selectivity for Electrocatalytic CO<sub>2</sub> Reduction. *ACS Catal.* **2015**, *5*, 4586–4591. [[CrossRef](#)]
50. Won, D.H.; Shin, H.; Koh, J.; Chung, J.; Lee, H.S.; Kim, H.; Woo, S.I. Highly Efficient, Selective, and Stable CO<sub>2</sub> Electroreduction on a Hexagonal Zn Catalyst. *Angew. Chem. Int. Ed.* **2016**, *55*, 9297–9300. [[CrossRef](#)] [[PubMed](#)]
51. Xiao, J.; Gao, M.R.; Liu, S.; Luo, J.L. Hexagonal Zn Nanoplates Enclosed by Zn(100) and Zn(002) Facets for Highly Selective CO<sub>2</sub> Electroreduction to CO. *ACS Appl. Mater. Interfaces* **2020**, *12*, 31431–31438. [[CrossRef](#)]
52. Luo, W.; Zhang, J.; Li, M.; Züttel, A. Boosting CO Production in Electrocatalytic CO<sub>2</sub> Reduction on Highly Porous Zn Catalysts. *ACS Catal.* **2019**, *9*, 3783–3791. [[CrossRef](#)]
53. Quan, F.; Zhong, D.; Song, H.; Jia, F.; Zhang, L. A highly efficient zinc catalyst for selective electroreduction of carbon dioxide in aqueous NaCl solution. *J. Mater. Chem. A* **2015**, *3*, 16409–16413. [[CrossRef](#)]
54. Li, Y.H.; Liu, P.F.; Li, C.; Yang, H.G. Sharp-Tipped Zinc Nanowires as an Efficient Electrocatalyst for Carbon Dioxide Reduction. *Chemistry* **2018**, *24*, 15486–15490. [[CrossRef](#)] [[PubMed](#)]

55. Jiang, X.; Cai, F.; Gao, D.; Dong, J.; Miao, S.; Wang, G.; Bao, X. Electrocatalytic reduction of carbon dioxide over reduced nanoporous zinc oxide. *Electrochem. Commun.* **2016**, *68*, 67–70. [CrossRef]
56. Nguyen, D.L.T.; Jee, M.S.; Won, D.H.; Jung, H.; Oh, H.-S.; Min, B.K.; Hwang, Y.J. Selective CO<sub>2</sub> Reduction on Zinc Electrocatalyst: The Effect of Zinc Oxidation State Induced by Pretreatment Environment. *ACS Sustain. Chem. Eng.* **2017**, *5*, 11377–11386. [CrossRef]
57. Jiang, K.; Wang, H.; Cai, W.B.; Wang, H. Li Electrochemical Tuning of Metal Oxide for Highly Selective CO<sub>2</sub> Reduction. *ACS Nano* **2017**, *11*, 6451–6458. [CrossRef] [PubMed]
58. Jeon, H.S.; Sinev, I.; Scholten, F.; Divins, N.J.; Zegkinoglou, I.; Pielsticker, L.; Cuenya, B.R. Operando Evolution of the Structure and Oxidation State of Size-Controlled Zn Nanoparticles during CO<sub>2</sub> Electroreduction. *J. Am. Chem. Soc.* **2018**, *140*, 9383–9386. [CrossRef]
59. Zhang, T.; Li, X.; Qiu, Y.; Su, P.; Xu, W.; Zhong, H.; Zhang, H. Multilayered Zn nanosheets as an electrocatalyst for efficient electrochemical reduction of CO<sub>2</sub>. *J. Catal.* **2018**, *357*, 154–162. [CrossRef]
60. Qin, B.; Li, Y.; Fu, H.; Wang, H.; Chen, S.; Liu, Z.; Peng, F. Electrochemical Reduction of CO<sub>2</sub> into Tunable Syngas Production by Regulating the Crystal Facets of Earth-Abundant Zn Catalyst. *ACS Appl. Mater. Interfaces* **2018**, *10*, 20530–20539. [CrossRef] [PubMed]
61. Morimoto, M.; Takatsuji, Y.; Hirata, K.; Fukuma, T.; Ohno, T.; Sakakura, T.; Haruyama, T. Visualization of catalytic edge reactivity in electrochemical CO<sub>2</sub> reduction on porous Zn electrode. *Electrochim. Acta* **2018**, *290*, 255–261. [CrossRef]
62. Liu, K.; Wang, J.; Shi, M.; Yan, J.; Jiang, Q. Simultaneous Achieving of High Faradaic Efficiency and CO Partial Current Density for CO<sub>2</sub> Reduction via Robust, Noble-Metal-Free Zn Nanosheets with Favorable Adsorption Energy. *Adv. Energy Mater.* **2019**, *9*, 1900276. [CrossRef]
63. Wang, J.; Zhu, Z.; Wei, X.; Li, Z.; Chen, J.S.; Wu, R.; Wei, Z. Hydrogen-Mediated Synthesis of 3D Hierarchical Porous Zinc Catalyst for CO<sub>2</sub> Electroreduction with High Current Density. *J. Phys. Chem. C* **2021**, *125*, 23784–23790. [CrossRef]
64. Wang, W.; He, X.; Zhang, K.; Yao, Y. Surfactant-modified Zn nanosheets on carbon paper for electrochemical CO<sub>2</sub> reduction to CO. *Chem. Commun.* **2022**, *58*, 5096–5099. [CrossRef] [PubMed]
65. Pan, H.; Wang, F.; She, S.; Zhang, Z.; Min, S. Boosting CO<sub>2</sub> electroreduction on a Zn electrode via concurrent surface reconstruction and interfacial surfactant modification. *Dalton Trans.* **2023**, *52*, 556–561. [CrossRef] [PubMed]
66. Fang, Y.; Yu, Y.; Zhao, W.; Yang, P.; Huang, T.; Gao, S. In situ Electrochemical Restructuring Integrating Corrosion Engineering to Fabricate Zn Nanosheets for Efficient CO<sub>2</sub> Electroreduction. *Electrocatalysis* **2022**, *14*, 29–38. [CrossRef]
67. Sun, Z.; Hu, Y.; Zhou, D.; Sun, M.; Wang, S.; Chen, W. Factors Influencing the Performance of Copper-Bearing Catalysts in the CO<sub>2</sub> Reduction System. *ACS Energy Lett.* **2021**, *6*, 3992–4022. [CrossRef]
68. Lim, H.K.; Shin, H.; Goddard, W.A., 3rd; Hwang, Y.J.; Min, B.K.; Kim, H. Embedding covalency into metal catalysts for efficient electrochemical conversion of CO<sub>2</sub>. *J. Am. Chem. Soc.* **2014**, *136*, 11355–11361. [CrossRef]
69. Hall, A.S.; Yoon, Y.; Wuttig, A.; Surendranath, Y. Mesostructure-Induced Selectivity in CO<sub>2</sub> Reduction Catalysis. *J. Am. Chem. Soc.* **2015**, *137*, 14834–14837. [CrossRef]
70. Yoon, Y.; Hall, A.S.; Surendranath, Y. Tuning of Silver Catalyst Mesostructure Promotes Selective Carbon Dioxide Conversion into Fuels. *Angew. Chem. Int. Ed.* **2016**, *55*, 15282–15286. [CrossRef]
71. Lei, F.; Liu, W.; Sun, Y.; Xu, J.; Liu, K.; Liang, L.; Yao, T.; Pan, B.; Wei, S.; Xie, Y. Metallic tin quantum sheets confined in graphene toward high-efficiency carbon dioxide electroreduction. *Nat. Commun.* **2016**, *7*, 12697. [CrossRef]
72. Mistry, H.; Reske, R.; Zeng, Z.; Zhao, Z.J.; Greeley, J.; Strasser, P.; Cuenya, B.R. Exceptional size-dependent activity enhancement in the electroreduction of CO<sub>2</sub> over Au nanoparticles. *J. Am. Chem. Soc.* **2014**, *136*, 16473–16476. [CrossRef]
73. Baruch, M.F.; Pander, J.E.; White, J.L.; Bocarsly, A.B. Mechanistic Insights into the Reduction of CO<sub>2</sub> on Tin Electrodes using in Situ ATR-IR Spectroscopy. *ACS Catal.* **2015**, *5*, 3148–3156. [CrossRef]
74. Pander, J.E.; Baruch, M.F.; Bocarsly, A.B. Probing the Mechanism of Aqueous CO<sub>2</sub> Reduction on Post-Transition-Metal Electrodes using ATR-IR Spectroelectrochemistry. *ACS Catal.* **2016**, *6*, 7824–7833. [CrossRef]
75. Gao, D.; Scholten, F.; Roldan Cuenya, B. Improved CO<sub>2</sub> Electroreduction Performance on Plasma-Activated Cu Catalysts via Electrolyte Design: Halide Effect. *ACS Catal.* **2017**, *7*, 5112–5120. [CrossRef]
76. Nguyen, D.L.T.; Jee, M.S.; Won, D.H.; Oh, H.-S.; Min, B.K.; Hwang, Y.J. Effect of halides on nanoporous Zn-based catalysts for highly efficient electroreduction of CO<sub>2</sub> to CO. *Catal. Commun.* **2018**, *114*, 109–113. [CrossRef]
77. Ma, Y.; Wang, J.; Yu, J.; Zhou, J.; Zhou, X.; Li, H.; He, Z.; Long, H.; Wang, Y.; Lu, P.; et al. Surface modification of metal materials for high-performance electrocatalytic carbon dioxide reduction. *Matter* **2021**, *4*, 888–926. [CrossRef]
78. Kim, C.; Eom, T.; Jee, M.S.; Jung, H.; Kim, H.; Min, B.K.; Hwang, Y.J. Insight into Electrochemical CO<sub>2</sub> Reduction on Surface-Molecule-Mediated Ag Nanoparticles. *ACS Catal.* **2016**, *7*, 779–785. [CrossRef]
79. Cao, Z.; Kim, D.; Hong, D.; Yu, Y.; Xu, J.; Lin, S.; Wen, X.; Nichols, E.M.; Jeong, K.; Reimer, J.A.; et al. A Molecular Surface Functionalization Approach to Tuning Nanoparticle Electrocatalysts for Carbon Dioxide Reduction. *J. Am. Chem. Soc.* **2016**, *138*, 8120–8125. [CrossRef]
80. Shinagawa, T.; Larrazábal, G.O.; Martín, A.J.; Krumeich, F.; Pérez-Ramírez, J. Sulfur-Modified Copper Catalysts for the Electrochemical Reduction of Carbon Dioxide to Formate. *ACS Catal.* **2018**, *8*, 837–844. [CrossRef]
81. Zhang, T.; Zhong, H.; Qiu, Y.; Li, X.; Zhang, H. Zn electrode with a layer of nanoparticles for selective electroreduction of CO<sub>2</sub> to formate in aqueous solutions. *J. Mater. Chem. A* **2016**, *4*, 16670–16676. [CrossRef]

82. Yadav, V.S.K.; Purkait, M.K. Electrochemical reduction of CO<sub>2</sub> to HCOOH using zinc and cobalt oxide as electrocatalysts. *New J. Chem.* **2015**, *39*, 7348–7354. [[CrossRef](#)]
83. Takatsuji, Y.; Morimoto, M.; Nakatsuru, Y.; Haruyama, T. Anodized Zn electrode for formate selectivity during the electrochemical reduction of CO<sub>2</sub> at low applied potential. *Electrochem. Commun.* **2022**, *138*, 107281. [[CrossRef](#)]
84. Jeon, H.S.; Timoshenko, J.; Scholten, F.; Sinev, I.; Herzog, A.; Haase, F.T.; Roldan Cuenya, B. Operando Insight into the Correlation between the Structure and Composition of CuZn Nanoparticles and Their Selectivity for the Electrochemical CO<sub>2</sub> Reduction. *J. Am. Chem. Soc.* **2019**, *141*, 19879–19887. [[CrossRef](#)] [[PubMed](#)]
85. Mosali, V.S.S.; Bond, A.M.; Zhang, J. Alloying strategies for tuning product selectivity during electrochemical CO<sub>2</sub> reduction over Cu. *Nanoscale* **2022**, *14*, 15560–15585. [[CrossRef](#)] [[PubMed](#)]
86. Ren, B.; Zhang, Z.; Wen, G.; Zhang, X.; Xu, M.; Weng, Y.; Nie, Y.; Dou, H.; Jiang, Y.; Deng, Y.P.; et al. Dual-Scale Integration Design of Sn-ZnO Catalyst toward Efficient and Stable CO<sub>2</sub> Electroreduction. *Adv. Mater.* **2022**, *34*, e2204637. [[CrossRef](#)] [[PubMed](#)]
87. Ajmal, S.; Yang, Y.; Li, K.; Tahir, M.A.; Liu, Y.; Wang, T.; Bacha, A.-U.-R.; Feng, Y.; Deng, Y.; Zhang, L. Zinc-Modified Copper Catalyst for Efficient (Photo-)Electrochemical CO<sub>2</sub> Reduction with High Selectivity of HCOOH Production. *J. Phys. Chem. C* **2019**, *123*, 11555–11563. [[CrossRef](#)]
88. Wu, Z.; Wu, H.; Cai, W.; Wen, Z.; Jia, B.; Wang, L.; Jin, W.; Ma, T. Engineering Bismuth-Tin Interface in Bimetallic Aerogel with a 3D Porous Structure for Highly Selective Electrocatalytic CO<sub>2</sub> Reduction to HCOOH. *Angew. Chem. Int. Ed.* **2021**, *60*, 12554–12559. [[CrossRef](#)]
89. Xie, L.; Liu, X.; Huang, F.; Liang, J.; Liu, J.; Wang, T.; Yang, L.; Cao, R.; Li, Q. Regulating Pd-catalysis for electrocatalytic CO<sub>2</sub> reduction to formate via intermetallic PdBi nanosheets. *Chin. J. Catal.* **2022**, *43*, 1680–1686. [[CrossRef](#)]
90. Zeng, J.; Fiorentin, M.R.; Fontana, M.; Castellino, M.; Risplendi, F.; Sacco, A.; Cicero, G.; Farkhondehfar, M.A.; Drago, F.; Pirri, C.F. Novel Insights into Sb-Cu Catalysts for Electrochemical Reduction of CO<sub>2</sub>. *Appl. Catal. B Environ.* **2022**, *306*, 121089. [[CrossRef](#)]
91. Wang, L.; Peng, H.; Lamaison, S.; Qi, Z.; Koshy, D.M.; Stevens, M.B.; Wakerley, D.; Zamora Zeledón, J.A.; King, L.A.; Zhou, L.; et al. Bimetallic effects on Zn-Cu electrocatalysts enhance activity and selectivity for the conversion of CO<sub>2</sub> to CO. *Chem. Catal.* **2021**, *1*, 663–680. [[CrossRef](#)]
92. Zeng, J.; Rino, T.; Bejtka, K.; Castellino, M.; Sacco, A.; Farkhondehfar, M.A.; Chiodoni, A.; Drago, F.; Pirri, C.F. Coupled Copper-Zinc Catalysts for Electrochemical Reduction of Carbon Dioxide. *ChemSusChem* **2020**, *13*, 4128–4139. [[CrossRef](#)] [[PubMed](#)]
93. Wan, L.; Zhang, X.; Cheng, J.; Chen, R.; Wu, L.; Shi, J.; Luo, J. Bimetallic Cu-Zn Catalysts for Electrochemical CO<sub>2</sub> Reduction: Phase-Separated versus Core-Shell Distribution. *ACS Catal.* **2022**, *12*, 2741–2748. [[CrossRef](#)]
94. Keerthiga, G.; Chetty, R. Electrochemical Reduction of Carbon Dioxide on Zinc-Modified Copper Electrodes. *J. Electrochem. Soc.* **2017**, *164*, H164–H169. [[CrossRef](#)]
95. Yin, G.; Abe, H.; Kodiyath, R.; Ueda, S.; Srinivasan, N.; Yamaguchi, A.; Miyauchi, M. Selective electro- or photo-reduction of carbon dioxide to formic acid using a Cu-Zn alloy catalyst. *J. Mater. Chem. A* **2017**, *5*, 12113–12119. [[CrossRef](#)]
96. Hu, H.; Tang, Y.; Hu, Q.; Wan, P.; Dai, L.; Yang, X.J. In-situ grown nanoporous Zn-Cu catalysts on brass foils for enhanced electrochemical reduction of carbon dioxide. *Appl. Surf. Sci.* **2018**, *445*, 281–286. [[CrossRef](#)]
97. Lamaison, S.; Wakerley, D.; Montero, D.; Rousse, G.; Taverna, D.; Giaume, D.; Mercier, D.; Blanchard, J.; Tran, H.N.; Fontecave, M.; et al. Zn-Cu Alloy Nanofoams as Efficient Catalysts for the Reduction of CO<sub>2</sub> to Syngas Mixtures with a Potential-Independent H<sub>2</sub>/CO Ratio. *ChemSusChem* **2019**, *12*, 511–517. [[CrossRef](#)] [[PubMed](#)]
98. Zhang, T.; Qiu, Y.; Yao, P.; Li, X.; Zhang, H. Bi-Modified Zn Catalyst for Efficient CO<sub>2</sub> Electrochemical Reduction to Formate. *ACS Sustain. Chem. Eng.* **2019**, *7*, 15190–15196. [[CrossRef](#)]
99. Kwon, I.S.; Debelo, T.T.; Kwak, I.H.; Seo, H.W.; Park, K.; Kim, D.; Yoo, S.J.; Kim, J.-G.; Park, J.; Kang, H.S. Selective electrochemical reduction of carbon dioxide to formic acid using indium-zinc bimetallic nanocrystals. *J. Mater. Chem. A* **2019**, *7*, 22879–22883. [[CrossRef](#)]
100. Li, W.; Zhang, Z.; Liu, W.; Gan, Q.; Liu, M.; Huo, S.; Chen, W. ZnSn nanocatalyst: Ultra-high formate selectivity from CO<sub>2</sub> electrochemical reduction and the structure evolution effect. *J. Colloid Interface Sci.* **2022**, *608 Pt 3*, 2791–2800. [[CrossRef](#)]
101. Gunji, T.; Ochiai, H.; Ohira, T.; Liu, Y.; Nakajima, Y.; Matsumoto, F. Preparation of Various Pd-Based Alloys for Electrocatalytic CO<sub>2</sub> Reduction Reaction-Selectivity Depending on Secondary Elements. *Chem. Mater.* **2020**, *32*, 6855–6863. [[CrossRef](#)]
102. Woyessa, G.W.; Chuang, C.H.; Rameez, M.; Hung, C.H. Electronic Structure Optimization of PdZn-Graphitic Carbon Nitride Nanocomposites as Electrocatalysts for Selective CO<sub>2</sub> to CO Conversion. *ACS Omega* **2022**, *7*, 17295–17304. [[CrossRef](#)]
103. Payra, S.; Shenoy, S.; Chakraborty, C.; Tarafder, K.; Roy, S. Structure-Sensitive Electrocatalytic Reduction of CO<sub>2</sub> to Methanol over Carbon-Supported Intermetallic PtZn Nano-Alloys. *ACS Appl. Mater. Interfaces* **2020**, *12*, 19402–19414. [[CrossRef](#)]
104. Liu, W.; Li, W.; Zhang, Z.; Cao, Z.; Huo, S. Zn-Sb Bimetallic Electrocatalyst Enhances the Conversion of CO<sub>2</sub> to Formate. *Chem. Asian J.* **2022**, *17*, e202200873. [[CrossRef](#)] [[PubMed](#)]
105. Zhang, X.; Zhou, Y.; Zhang, H.; Li, H.; Liu, K.; Li, H.; Pan, H.; Hu, J.; Fu, J.; Chen, S.; et al. Tuning the electron structure enables the NiZn alloy for CO<sub>2</sub> electroreduction to formate. *J. Energy Chem.* **2021**, *63*, 625–632. [[CrossRef](#)]
106. Liu, W.; Zhang, Z.; Huo, S.; Ren, Q.; Liu, M. Bimetallic Zn<sub>3</sub>Sn<sub>2</sub> electrocatalyst derived from mixed oxides enhances formate production towards CO<sub>2</sub> electroreduction reaction. *Appl. Surf. Sci.* **2023**, *608*, 155110. [[CrossRef](#)]
107. Badawy, I.M.; Ismail, A.M.; Khedr, G.E.; Taha, M.M.; Allam, N.K. Selective electrochemical reduction of CO<sub>2</sub> on compositionally variant bimetallic Cu-Zn electrocatalysts derived from scrap brass alloys. *Sci. Rep.* **2022**, *12*, 13456. [[CrossRef](#)]

108. Mosali, V.S.S.; Zhang, X.; Zhang, Y.; Gengenbach, T.; Guo, S.-X.; Puxty, G.; Horne, M.D.; Bond, A.M.; Zhang, J. Electrocatalytic CO<sub>2</sub> Reduction to Formate on Cu Based Surface Alloys with Enhanced Selectivity. *ACS Sustain. Chem. Eng.* **2019**, *7*, 19453–19462. [[CrossRef](#)]
109. Huang, Y.P.; Tung, C.W.; Chen, T.L.; Hsu, C.S.; Liao, M.Y.; Chen, H.C.; Chen, H.M. In situ probing the dynamic reconstruction of copper-zinc electrocatalysts for CO<sub>2</sub> reduction. *Nanoscale* **2022**, *14*, 8944–8950. [[CrossRef](#)]
110. Feng, Y.; Li, Z.; Liu, H.; Dong, C.; Wang, J.; Kulinich, S.A.; Du, X. Laser-Prepared CuZn Alloy Catalyst for Selective Electrochemical Reduction of CO<sub>2</sub> to Ethylene. *Langmuir* **2018**, *34*, 13544–13549. [[CrossRef](#)]
111. Su, X.; Sun, Y.; Jin, L.; Zhang, L.; Yang, Y.; Kerns, P.; Liu, B.; Li, S.; He, J. Hierarchically porous Cu/Zn bimetallic catalysts for highly selective CO<sub>2</sub> electroreduction to liquid C<sub>2</sub> products. *Appl. Catal. B Environ.* **2020**, *269*, 118800. [[CrossRef](#)]
112. Juntrapirom, S.; Santatiwongchai, J.; Watwiangkham, A.; Suthirakun, S.; Butburee, T.; Faungnawakij, K.; Chakthranont, P.; Hirunsit, P.; Rungtaweeworant, B. Tuning CuZn interfaces in metal-organic framework-derived electrocatalysts for enhancement of CO<sub>2</sub> conversion to C<sub>2</sub> products. *Catal. Sci. Technol.* **2021**, *11*, 8065–8078. [[CrossRef](#)]
113. Da Silva, A.H.M.; Raaijman, S.J.; Santana, C.S.; Assaf, J.M.; Gomes, J.F.; Koper, M.T.M. Electrocatalytic CO<sub>2</sub> reduction to C<sub>2+</sub> products on Cu and Cu<sub>x</sub>Zn<sub>y</sub> electrodes: Effects of chemical composition and surface morphology. *J. Electroanal. Chem.* **2021**, *880*, 114750. [[CrossRef](#)]
114. Lamaison, S.; Wakerley, D.; Kracke, F.; Moore, T.; Zhou, L.; Lee, D.U.; Wang, L.; Hubert, M.A.; Aviles Acosta, J.E.; Gregoire, J.M.; et al. Designing a Zn-Ag Catalyst Matrix and Electrolyzer System for CO<sub>2</sub> Conversion to CO and Beyond. *Adv. Mater.* **2022**, *34*, e2103963. [[CrossRef](#)]
115. Hatsukade, T.; Kuhl, K.P.; Cave, E.R.; Abram, D.N.; Feaster, J.T.; Jongorius, A.L.; Hahn, C.; Jaramillo, T.F. Carbon Dioxide Electroreduction using a Silver–Zinc Alloy. *Energy Technol.* **2017**, *5*, 955–961. [[CrossRef](#)]
116. Zhou, Y.; Ni, G.; Wu, K.; Chen, Q.; Wang, X.; Zhu, W.; He, Z.; Li, H.; Fu, J.; Liu, M. Porous Zn Conformal Coating on Dendritic-Like Ag with Enhanced Selectivity and Stability for CO<sub>2</sub> Electroreduction to CO. *Adv. Sustain. Syst.* **2022**, *7*, 2200374. [[CrossRef](#)]
117. Jo, A.; Kim, S.; Park, H.; Park, H.-Y.; Hyun Jang, J.; Park, H.S. Enhanced electrochemical conversion of CO<sub>2</sub> to CO at bimetallic Ag-Zn catalysts formed on polypyrrole-coated electrode. *J. Catal.* **2021**, *393*, 92–99. [[CrossRef](#)]
118. Lamaison, S.; Wakerley, D.; Blanchard, J.; Montero, D.; Rousse, G.; Mercier, D.; Marcus, P.; Taverna, D.; Giaume, D.; Mougél, V.; et al. High-Current-Density CO<sub>2</sub>-to-CO Electroreduction on Ag-Alloyed Zn Dendrites at Elevated Pressure. *Joule* **2020**, *4*, 395–406. [[CrossRef](#)]
119. Moreno-Garcia, P.; Schlegel, N.; Zanetti, A.; Cedeno Lopez, A.; Galvez-Vazquez, M.J.; Dutta, A.; Rahaman, M.; Broekmann, P. Selective Electrochemical Reduction of CO<sub>2</sub> to CO on Zn-Based Foams Produced by Cu<sup>2+</sup> and Template-Assisted Electrodeposition. *ACS Appl. Mater. Interfaces* **2018**, *10*, 31355–31365. [[CrossRef](#)]
120. Guo, W.; Shim, K.; Kim, Y.-T. Ag layer deposited on Zn by physical vapor deposition with enhanced CO selectivity for electrochemical CO<sub>2</sub> reduction. *Appl. Surf. Sci.* **2020**, *526*, 146651. [[CrossRef](#)]
121. Albo, J.; Sáez, A.; Solla-Gullón, J.; Montiel, V.; Irabien, A. Production of methanol from CO<sub>2</sub> electroreduction at Cu<sub>2</sub>O and Cu<sub>2</sub>O/ZnO-based electrodes in aqueous solution. *Appl. Catal. B Environ.* **2015**, *176–177*, 709–717. [[CrossRef](#)]
122. Tan, D.; Lee, W.; Kim, Y.E.; Ko, Y.N.; Youn, M.H.; Jeon, Y.E.; Hong, J.; Jeong, S.K.; Park, K.T. SnO<sub>2</sub>/ZnO Composite Hollow Nanofiber Electrocatalyst for Efficient CO<sub>2</sub> Reduction to Formate. *ACS Sustain. Chem. Eng.* **2020**, *8*, 10639–10645. [[CrossRef](#)]
123. Ren, D.; Ang, B.S.-H.; Yeo, B.S. Tuning the Selectivity of Carbon Dioxide Electroreduction toward Ethanol on Oxide-Derived Cu<sub>x</sub>Zn Catalysts. *ACS Catal.* **2016**, *6*, 8239–8247. [[CrossRef](#)]
124. Albo, J.; Irabien, A. Cu<sub>2</sub>O-loaded gas diffusion electrodes for the continuous electrochemical reduction of CO<sub>2</sub> to methanol. *J. Catal.* **2016**, *343*, 232–239. [[CrossRef](#)]
125. Li, Z.; Yadav, R.M.; Sun, L.; Zhang, T.; Zhang, J.; Ajayan, P.M.; Wu, J. CuO/ZnO/C electrocatalysts for CO<sub>2</sub>-to-C<sub>2+</sub> products conversion with high yield: On the effect of geometric structure and composition. *Appl. Catal. A Gen.* **2020**, *606*, 117829. [[CrossRef](#)]
126. Dongare, S.; Singh, N.; Bhunia, H. Oxide-derived Cu-Zn nanoparticles supported on N-doped graphene for electrochemical reduction of CO<sub>2</sub> to ethanol. *Appl. Surf. Sci.* **2021**, *556*, 149790. [[CrossRef](#)]
127. Zhang, T.; Li, Z.; Zhang, J.; Wu, J. Enhance CO<sub>2</sub>-to-C<sub>2+</sub> products yield through spatial management of CO transport in Cu/ZnO tandem electrodes. *J. Catal.* **2020**, *387*, 163–169. [[CrossRef](#)]
128. Dongare, S.; Singh, N.; Bhunia, H.; Bajpai, P.K. Electrochemical reduction of CO<sub>2</sub> using oxide based Cu and Zn bimetallic catalyst. *Electrochim. Acta* **2021**, *392*, 138988. [[CrossRef](#)]
129. Zoubir, O.; Atourki, L.; Ait Ahsaine, H.; BaQais, A. Current state of copper-based bimetallic materials for electrochemical CO<sub>2</sub> reduction: A review. *RSC Adv.* **2022**, *12*, 30056–30075. [[CrossRef](#)] [[PubMed](#)]
130. Wang, J.; Li, Z.; Dong, C.; Feng, Y.; Yang, J.; Liu, H.; Du, X. Silver/Copper Interface for Relay Electroreduction of Carbon Dioxide to Ethylene. *ACS Appl. Mater. Interfaces* **2019**, *11*, 2763–2767. [[CrossRef](#)]
131. Manthiram, K.; Beberwyck, B.J.; Alivisatos, A.P. Enhanced electrochemical methanation of carbon dioxide with a dispersible nanoscale copper catalyst. *J. Am. Chem. Soc.* **2014**, *136*, 13319–13325. [[CrossRef](#)]
132. Reske, R.; Mistry, H.; Behafarid, F.; Roldan Cuenya, B.; Strasser, P. Particle Size Effects in the Catalytic Electroreduction of CO<sub>2</sub> on Cu Nanoparticles. *J. Am. Chem. Soc.* **2014**, *136*, 6978–6986. [[CrossRef](#)] [[PubMed](#)]
133. Nitopi, S.; Bertheussen, E.; Scott, S.B.; Liu, X.; Engstfeld, A.K.; Horch, S.; Seger, B.; Stephens, I.E.L.; Chan, K.; Hahn, C.; et al. Progress and Perspectives of Electrochemical CO<sub>2</sub> Reduction on Copper in Aqueous Electrolyte. *Chem. Rev.* **2019**, *119*, 7610–7672. [[CrossRef](#)]

134. Montoya, J.H.; Shi, C.; Chan, K.; Norskov, J.K. Theoretical Insights into a CO Dimerization Mechanism in CO<sub>2</sub> Electroreduction. *J. Phys. Chem. Lett.* **2015**, *6*, 2032–2037. [[CrossRef](#)] [[PubMed](#)]
135. Timoshenko, J.; Jeon, H.S.; Sinev, I.; Haase, F.T.; Herzog, A.; Roldan Cuenya, B. Linking the evolution of catalytic properties and structural changes in copper-zinc nanocatalysts using operando EXAFS and neural-networks. *Chem. Sci.* **2020**, *11*, 3727–3736. [[CrossRef](#)] [[PubMed](#)]
136. Sun, D.; Xu, X.; Qin, Y.; Jiang, S.P.; Shao, Z. Rational Design of Ag-Based Catalysts for the Electrochemical CO<sub>2</sub> Reduction to CO: A Review. *ChemSusChem* **2020**, *13*, 39–58. [[CrossRef](#)]
137. Sun, J.; Yu, B.; Yan, X.; Wang, J.; Tan, F.; Yang, W.; Cheng, G.; Zhang, Z. High Throughput Preparation of Ag-Zn Alloy Thin Films for the Electrocatalytic Reduction of CO<sub>2</sub> to CO. *Mater.* **2022**, *15*, 6892. [[CrossRef](#)]
138. Yang, B.; Liu, K.; Li, H.; Liu, C.; Fu, J.; Li, H.; Huang, J.E.; Ou, P.; Alkayali, T.; Cai, C.; et al. Accelerating CO<sub>2</sub> Electroreduction to Multicarbon Products via Synergistic Electric-Thermal Field on Copper Nanoneedles. *J. Am. Chem. Soc.* **2022**, *144*, 3039–3049. [[CrossRef](#)]
139. Zhou, Y.; Liang, Y.; Fu, J.; Liu, K.; Chen, Q.; Wang, X.; Li, H.; Zhu, L.; Hu, J.; Pan, H.; et al. Vertical Cu Nanoneedle Arrays Enhance the Local Electric Field Promoting C<sub>2</sub> Hydrocarbons in the CO<sub>2</sub> Electroreduction. *Nano Lett.* **2022**, *22*, 1963–1970. [[CrossRef](#)]
140. Gao, D.; Zhou, H.; Cai, F.; Wang, D.; Hu, Y.; Jiang, B.; Cai, W.-B.; Chen, X.; Si, R.; Yang, F.; et al. Switchable CO<sub>2</sub> electroreduction via engineering active phases of Pd nanoparticles. *Nano Res.* **2017**, *10*, 2181–2191. [[CrossRef](#)]
141. Zeng, J.; Zhang, W.; Yang, Y.; Li, D.; Yu, X.; Gao, Q. Pd-Ag Alloy Electrocatalysts for CO<sub>2</sub> Reduction: Composition Tuning to Break the Scaling Relationship. *ACS Appl. Mater. Interfaces* **2019**, *11*, 33074–33081. [[CrossRef](#)]
142. Xue, D.; Xia, H.; Yan, W.; Zhang, J.; Mu, S. Defect Engineering on Carbon-Based Catalysts for Electrocatalytic CO<sub>2</sub> Reduction. *Nanomicro Lett.* **2020**, *13*, 5. [[CrossRef](#)] [[PubMed](#)]
143. Back, S.; Kim, H.; Jung, Y. Selective Heterogeneous CO<sub>2</sub> Electroreduction to Methanol. *ACS Catal.* **2015**, *5*, 965–971. [[CrossRef](#)]
144. Li, F.; Chen, L.; Knowles, G.P.; MacFarlane, D.R.; Zhang, J. Hierarchical Mesoporous SnO<sub>2</sub> Nanosheets on Carbon Cloth: A Robust and Flexible Electrocatalyst for CO<sub>2</sub> Reduction with High Efficiency and Selectivity. *Angew. Chem. Int. Ed.* **2017**, *56*, 505–509. [[CrossRef](#)]
145. Chen, Y.; Kanan, M.W. Tin oxide dependence of the CO<sub>2</sub> reduction efficiency on tin electrodes and enhanced activity for tin/tin oxide thin-film catalysts. *J. Am. Chem. Soc.* **2012**, *134*, 1986–1989. [[CrossRef](#)]
146. An, X.; Li, S.; Yoshida, A.; Wang, Z.; Hao, X.; Abudula, A.; Guan, G. Electrodeposition of Tin-Based Electrocatalysts with Different Surface Tin Species Distributions for Electrochemical Reduction of CO<sub>2</sub> to HCOOH. *ACS Sustain. Chem. Eng.* **2019**, *7*, 9360–9368. [[CrossRef](#)]
147. Nellaiappan, S.; Sharma, S. Substitution of Zinc(II) in Nickel(II) Oxide as Proficient Copper-Free Catalysts for Selective CO<sub>2</sub> Electroreduction. *ACS Appl. Energy Mater.* **2019**, *2*, 2998–3003. [[CrossRef](#)]
148. Song, Y.; Wang, Y.; Shao, J.; Ye, K.; Wang, Q.; Wang, G. Boosting CO<sub>2</sub> Electroreduction via Construction of a Stable ZnS/ZnO Interface. *ACS Appl. Mater. Interfaces* **2022**, *14*, 20368–20374. [[CrossRef](#)] [[PubMed](#)]
149. Ren, X.; Gao, Y.; Zheng, L.; Wang, Z.; Wang, P.; Zheng, Z.; Liu, Y.; Cheng, H.; Dai, Y.; Huang, B. Oxygen vacancy enhancing CO<sub>2</sub> electrochemical reduction to CO on Ce-doped ZnO catalysts. *Surf. Interfaces* **2021**, *23*, 100923. [[CrossRef](#)]
150. Luo, W.; Zhang, Q.; Zhang, J.; Moiola, E.; Zhao, K.; Züttel, A. Electrochemical reconstruction of ZnO for selective reduction of CO<sub>2</sub> to CO. *Appl. Catal. B Environ.* **2020**, *273*, 119060. [[CrossRef](#)]
151. Lü, F.; Bao, H.; He, F.; Qi, G.; Sun, J.; Zhang, S.; Zhuo, L.; Yang, H.; Hu, G.; Luo, J.; et al. Nitrogen dopant induced highly selective CO<sub>2</sub> reduction over lotus-leaf shaped ZnO nanorods. *Mater. Chem. Front.* **2021**, *5*, 4225–4230. [[CrossRef](#)]
152. Xiang, Q.; Li, F.; Wang, J.; Chen, W.; Miao, Q.; Zhang, Q.; Tao, P.; Song, C.; Shang, W.; Zhu, H.; et al. Heterostructure of ZnO Nanosheets/Zn with a Highly Enhanced Edge Surface for Efficient CO<sub>2</sub> Electrochemical Reduction to CO. *ACS Appl. Mater. Interfaces* **2021**, *13*, 10837–10844. [[CrossRef](#)] [[PubMed](#)]
153. Wang, H.; Xiao, Y.; Qi, Y.; Zhang, A.; Du, J.; Li, J.; Guo, T. Fabrication of ZnO nanosheets self-assembled by nanoparticles for accelerated electrocatalytic reduction of CO<sub>2</sub> to CO. *Fuel* **2023**, *333*, 126431. [[CrossRef](#)]
154. Huygh, S.; Bogaerts, A.; Neyts, E.C. How Oxygen Vacancies Activate CO<sub>2</sub> Dissociation on TiO<sub>2</sub> Anatase (001). *J. Phys. Chem. C* **2016**, *120*, 21659–21669. [[CrossRef](#)]
155. Geng, Z.; Kong, X.; Chen, W.; Su, H.; Liu, Y.; Cai, F.; Wang, G.; Zeng, J. Oxygen Vacancies in ZnO Nanosheets Enhance CO<sub>2</sub> Electrochemical Reduction to CO. *Angew. Chem. Int. Ed.* **2018**, *57*, 6054–6059. [[CrossRef](#)] [[PubMed](#)]
156. Zong, X.; Jin, Y.; Li, Y.; Zhang, X.; Zhang, S.; Xie, H.; Zhang, J.; Xiong, Y. Morphology-controllable ZnO catalysts enriched with oxygen-vacancies for boosting CO<sub>2</sub> electroreduction to CO. *J. CO<sub>2</sub> Util.* **2022**, *61*, 102051. [[CrossRef](#)]
157. Xue, L.; Zhang, A.; Wu, J.; Wang, Q.; Liu, Y.; Zhao, Y.; Liu, S.; Liu, Z.; Li, P.; Zeng, S. Surface modification and reconstruction of ZnO hollow microspheres for selective electroreduction of CO<sub>2</sub> to CO. *J. Alloys Compd.* **2021**, *882*, 160703. [[CrossRef](#)]
158. Kanase, R.S.; Arunachalam, M.; Badiger, J.; Das, P.K.; Kang, S.H. Highly Selective and Durable CO Production via Effective Morphology and Surface Engineering of ZnO Electrocatalysts. *ACS Appl. Energy Mater.* **2022**, *5*, 13913–13927. [[CrossRef](#)]
159. van Spronsen, M.A.; Frenken, J.W.M.; Groot, I.M.N. Surface science under reaction conditions: CO oxidation on Pt and Pd model catalysts. *Chem. Soc. Rev.* **2017**, *46*, 4347–4374. [[CrossRef](#)]
160. Sun, Q.; Jia, C.; Zhao, Y.; Zhao, C. Single atom-based catalysts for electrochemical CO<sub>2</sub> reduction. *Chin. J. Catal.* **2022**, *43*, 1547–1597. [[CrossRef](#)]

161. Zhang, J.; Cai, W.; Hu, F.X.; Yang, H.; Liu, B. Recent advances in single atom catalysts for the electrochemical carbon dioxide reduction reaction. *Chem. Sci.* **2021**, *12*, 6800–6819. [[CrossRef](#)]
162. Creissen, C.E.; Fontecave, M. Keeping sight of copper in single-atom catalysts for electrochemical carbon dioxide reduction. *Nat. Commun.* **2022**, *13*, 2280. [[CrossRef](#)] [[PubMed](#)]
163. Qu, Q.; Ji, S.; Chen, Y.; Wang, D.; Li, Y. The atomic-level regulation of single-atom site catalysts for the electrochemical CO<sub>2</sub> reduction reaction. *Chem. Sci.* **2021**, *12*, 4201–4215. [[CrossRef](#)]
164. Qu, G.; Wei, K.; Pan, K.; Qin, J.; Lv, J.; Li, J.; Ning, P. Emerging materials for electrochemical CO<sub>2</sub> reduction: Progress and optimization strategies of carbon-based single-atom catalysts. *Nanoscale* **2023**, *15*, 3666–3692. [[CrossRef](#)] [[PubMed](#)]
165. Gu, J.; Bai, L.; Chen, H.M.; Hu, X. Atomically dispersed Fe<sup>3+</sup> sites catalyze efficient CO<sub>2</sub> electroreduction to CO. *Science* **2019**, *364*, 1091–1094.
166. Wang, Y.; Jiang, Z.; Zhang, X.; Niu, Z.; Zhou, Q.; Wang, X.; Li, H.; Lin, Z.; Zheng, H.; Liang, Y. Metal Phthalocyanine-Derived Single-Atom Catalysts for Selective CO<sub>2</sub> Electroreduction under High Current Densities. *ACS Appl. Mater. Interfaces* **2020**, *12*, 33795–33802. [[CrossRef](#)] [[PubMed](#)]
167. Li, S.; Zhao, S.; Lu, X.; Ceccato, M.; Hu, X.M.; Roldan, A.; Catalano, J.; Liu, M.; Skrydstrup, T.; Daasbjerg, K. Low-Valence Zn<sup>δ+</sup> (0<δ<2) Single-Atom Material as Highly Efficient Electrocatalyst for CO<sub>2</sub> Reduction. *Angew. Chem. Int. Ed.* **2021**, *60*, 22826–22832.
168. Yang, F.; Song, P.; Liu, X.; Mei, B.; Xing, W.; Jiang, Z.; Gu, L.; Xu, W. Highly Efficient CO<sub>2</sub> Electroreduction on ZnN<sub>4</sub>-based Single-Atom Catalyst. *Angew. Chem. Int. Ed.* **2018**, *57*, 12303–12307. [[CrossRef](#)]
169. Wang, N.; Liu, Z.; Ma, J.; Liu, J.; Zhou, P.; Chao, Y.; Ma, C.; Bo, X.; Liu, J.; Hei, Y.; et al. Sustainability Perspective-Oriented Synthetic Strategy for Zinc Single-Atom Catalysts Boosting Electrocatalytic Reduction of Carbon Dioxide and Oxygen. *ACS Sustain. Chem. Eng.* **2020**, *8*, 13813–13822. [[CrossRef](#)]
170. Han, L.; Song, S.; Liu, M.; Yao, S.; Liang, Z.; Cheng, H.; Ren, Z.; Liu, W.; Lin, R.; Qi, G.; et al. Stable and Efficient Single-Atom Zn Catalyst for CO<sub>2</sub> Reduction to CH<sub>4</sub>. *J. Am. Chem. Soc.* **2020**, *142*, 12563–12567. [[CrossRef](#)]
171. Fang, M.; Wang, X.; Li, X.; Zhu, Y.; Xiao, G.; Feng, J.; Jiang, X.; Lv, K.; Zhu, Y.; Lin, W.F. Curvature-induced Zn 3d Electron Return on Zn-N<sub>4</sub> Single-atom Carbon Nanofibers for Boosting Electroreduction of CO<sub>2</sub>. *ChemCatChem* **2020**, *13*, 603–609. [[CrossRef](#)]
172. Hao, Z.; Chen, J.; Zhang, D.; Zheng, L.; Li, Y.; Yin, Z.; He, G.; Jiao, L.; Wen, Z.; Lv, X.J. Coupling effects of Zn single atom and high curvature supports for improved performance of CO<sub>2</sub> reduction. *Sci. Bull.* **2021**, *66*, 1649–1658. [[CrossRef](#)] [[PubMed](#)]
173. Lin, L.; Liu, T.; Xiao, J.; Li, H.; Wei, P.; Gao, D.; Nan, B.; Si, R.; Wang, G.; Bao, X. Enhancing CO<sub>2</sub> Electroreduction to Methane with a Cobalt Phthalocyanine and Zinc-Nitrogen-Carbon Tandem Catalyst. *Angew. Chem. Int. Ed.* **2020**, *59*, 22408–22413. [[CrossRef](#)]
174. Qiu, N.; Li, J.; Wang, H.; Zhang, Z. Emerging dual-atomic-site catalysts for electrocatalytic CO<sub>2</sub> reduction. *Sci. China Mater.* **2022**, *65*, 3302–3323. [[CrossRef](#)]
175. Zhu, W.; Zhang, L.; Liu, S.; Li, A.; Yuan, X.; Hu, C.; Zhang, G.; Deng, W.; Zang, K.; Luo, J.; et al. Enhanced CO<sub>2</sub> Electroreduction on Neighboring Zn/Co Monomers by Electronic Effect. *Angew. Chem. Int. Ed.* **2020**, *59*, 12664–12668. [[CrossRef](#)] [[PubMed](#)]
176. Zhong Liang, L.S. Mingzi Sun, Bolong Huang, Yaping Du, Tunable CO/H<sub>2</sub> ratios of electrochemical reduction of CO<sub>2</sub> through the Zn-Ln dual atomic catalysts. *Sci. Adv.* **2021**, *7*, eabl4915. [[CrossRef](#)]
177. Meng, L.; Zhang, E.; Peng, H.; Wang, Y.; Wang, D.; Rong, H.; Zhang, J. Bi/Zn Dual Single-Atom Catalysts for Electroreduction of CO<sub>2</sub> to Syngas. *ChemCatChem* **2022**, *14*, e202101801. [[CrossRef](#)]
178. Wang, H.; Yu, Z.; Zhou, J.; Li, C.; Jayanarasimhan, A.; Zhao, X.; Zhang, H. A Scientometric Review of CO<sub>2</sub> Electroreduction Research from 2005 to 2022. *Energies* **2023**, *16*, 616. [[CrossRef](#)]
179. Song, X.; Xu, L.; Sun, X.; Han, B. In situ/operando characterization techniques for electrochemical CO<sub>2</sub> reduction. *Sci. China Chem.* **2023**, *66*, 315–323. [[CrossRef](#)]
180. Zheng, M.; Wang, P.; Zhi, X.; Yang, K.; Jiao, Y.; Duan, J.; Zheng, Y.; Qiao, S.Z. Electrocatalytic CO<sub>2</sub>-to-C<sub>2+</sub> with Ampere-Level Current on Heteroatom-Engineered Copper via Tuning \*CO Intermediate Coverage. *J. Am. Chem. Soc.* **2022**, *144*, 14936–14944. [[CrossRef](#)]
181. Kang, M.P.L.; Kolb, M.J.; Calle-Vallejo, F.; Yeo, B.S. The Role of Undercoordinated Sites on Zinc Electrodes for CO<sub>2</sub> Reduction to CO. *Adv. Funct. Mater.* **2022**, *32*, 2111597. [[CrossRef](#)]
182. García de Arquer, F.P.; Dinh, C.-T.; Ozden, A.; Wicks, J.; McCallum, C.; Kirmani, A.R.; Nam, D.-H.; Gabardo, C.; Seifitokaldani, A.; Wang, X.; et al. CO<sub>2</sub> electrolysis to multicarbon products at activities greater than 1 A·cm<sup>-2</sup>. *Science* **2020**, *367*, 661–666. [[CrossRef](#)] [[PubMed](#)]
183. Ren, S.; Joulié, D.; Salvatore, D.; Torbensen, K.; Wang, M.; Robert, M.; Berlinguette, C.P. Molecular electrocatalysts can mediate fast, selective CO<sub>2</sub> reduction in a flow cell. *Science* **2019**, *365*, 367–369. [[CrossRef](#)] [[PubMed](#)]
184. Seong, H.; Efremov, V.; Park, G.; Kim, H.; Yoo, J.S.; Lee, D. Atomically Precise Gold Nanoclusters as Model Catalysts for Identifying Active Sites for Electroreduction of CO<sub>2</sub>. *Angew. Chem. Int. Ed.* **2021**, *60*, 14563–14570. [[CrossRef](#)]
185. Kim, B.; Seong, H.; Song, J.T.; Kwak, K.; Song, H.; Tan, Y.C.; Park, G.; Lee, D.; Oh, J. Over a 15.9% Solar-to-CO Conversion from Dilute CO<sub>2</sub> Streams Catalyzed by Gold Nanoclusters Exhibiting a High CO<sub>2</sub> Binding Affinity. *ACS Energy Lett.* **2019**, *5*, 749–757. [[CrossRef](#)]
186. Kutz, R.B.; Chen, Q.; Yang, H.; Sajjad, S.D.; Liu, Z.; Masel, I.R. Sustainion Imidazolium-Functionalized Polymers for Carbon Dioxide Electrolysis. *Energy Technol.* **2017**, *5*, 929–936. [[CrossRef](#)]
187. Haas, T.; Krause, R.; Weber, R.; Demler, M.; Schmid, G. Technical photosynthesis involving CO<sub>2</sub> electrolysis and fermentation. *Nat. Catal.* **2018**, *1*, 32–39. [[CrossRef](#)]

188. Kim, B.; Hillman, F.; Ariyoshi, M.; Fujikawa, S.; Kenis, P.J.A. Effects of composition of the micro porous layer and the substrate on performance in the electrochemical reduction of CO<sub>2</sub> to CO. *J. Power Sources* **2016**, *312*, 192–198. [[CrossRef](#)]
189. Ma, S.; Luo, R.; Gold, J.I.; Yu, A.Z.; Kim, B.; Kenis, P.J.A. Carbon nanotube containing Ag catalyst layers for efficient and selective reduction of carbon dioxide. *J. Mater. Chem. A* **2016**, *4*, 8573–8578. [[CrossRef](#)]
190. Gabardo, C.M.; Seifitokaldani, A.; Edwards, J.P.; Dinh, C.-T.; Burdyny, T.; Kibria, M.G.; O'Brien, C.P.; Sargent, E.H.; Sinton, D. Combined high alkalinity and pressurization enable efficient CO<sub>2</sub> electroreduction to CO. *Energy Environ. Sci.* **2018**, *11*, 2531–2539. [[CrossRef](#)]
191. Wang, R.; Haspel, H.; Pustovarenko, A.; Dikhtiarenko, A.; Russkikh, A.; Shterk, G.; Osadchii, D.; Ould-Chikh, S.; Ma, M.; Smith, W.A.; et al. Maximizing Ag Utilization in High-Rate CO<sub>2</sub> Electrochemical Reduction with a Coordination Polymer-Mediated Gas Diffusion Electrode. *ACS Energy Lett.* **2019**, *4*, 2024–2031. [[CrossRef](#)]
192. Dinh, C.-T.; Burdyny, T.; Kibria, M.G.; Seifitokaldani, A.; Gabardo, C.M.; García de Arquer, F.P.; Kiani, A.; Edwards, J.P.; De Luna, P.; Bushuyev, O.S.; et al. CO<sub>2</sub> electroreduction to ethylene via hydroxide-mediated copper catalysis at an abrupt interface. *Science* **2018**, *360*, 783–787. [[CrossRef](#)]
193. Li, F.; Thevenon, A.; Rosas-Hernandez, A.; Wang, Z.; Li, Y.; Gabardo, C.M.; Ozden, A.; Dinh, C.T.; Li, J.; Wang, Y.; et al. Molecular tuning of CO<sub>2</sub>-to-ethylene conversion. *Nature* **2020**, *577*, 509–513. [[CrossRef](#)] [[PubMed](#)]
194. Wei, P.; Gao, D.; Liu, T.; Li, H.; Sang, J.; Wang, C.; Cai, R.; Wang, G.; Bao, X. Coverage-driven selectivity switch from ethylene to acetate in high-rate CO<sub>2</sub>/CO electrolysis. *Nat. Nanotechnol.* **2023**, *18*, 299–306. [[CrossRef](#)]
195. Zhu, C.; Song, Y.; Dong, X.; Li, G.; Chen, A.; Chen, W.; Wu, G.; Li, S.; Wei, W.; Sun, Y. Ampere-level CO<sub>2</sub> reduction to multicarbon products over a copper gas penetration electrode. *Energy Environ. Sci.* **2022**, *15*, 5391–5404. [[CrossRef](#)]
196. Li, H.; Liu, T.; Wei, P.; Lin, L.; Gao, D.; Wang, G.; Bao, X. High-Rate CO<sub>2</sub> Electroreduction to C<sub>2+</sub> Products over a Copper-Copper Iodide Catalyst. *Angew. Chem. Int. Ed.* **2021**, *60*, 14329–14333. [[CrossRef](#)] [[PubMed](#)]

**Disclaimer/Publisher's Note:** The statements, opinions and data contained in all publications are solely those of the individual author(s) and contributor(s) and not of MDPI and/or the editor(s). MDPI and/or the editor(s) disclaim responsibility for any injury to people or property resulting from any ideas, methods, instructions or products referred to in the content.